Astronomy & Astrophysics manuscript no. 44040final
July 22, 2022
©ESO 2022

The Cygnus Allscale Survey of Chemistry and Dynamical Environments: CASCADE.

Overview and first results toward DR20 from the Max Planck IRAM Observatory program (MIOP)⋆.

H. Beuther[1], F. Wyrowski[2], K. M. Menten[2], J. M. Winters[3], S. Suri[1,4], W.-J. Kim[5], L. Bouscasse[3], C. Gieser[1], M. Sawczuck[1], I. B. Christensen[2], and I. M. Skretas[2]

[1] Max Planck Institute for Astronomy, Königstuhl 17, 69117 Heidelberg, Germany, e-mail: name@mpia.de
[2] Max-Planck-Institut für Radioastronomie, Auf dem Hügel 69, 53121 Bonn, Germany
[3] IRAM, 300 rue de la Piscine, Domaine Universitaire de Grenoble, 38406 St.-Martin-d'Hères, France
[4] Department of Astrophysics, University of Vienna, Türkenschanzstrasse 17,1180 Vienna, Austria
[5] I. Physikalisches Institut, Universität zu Köln, Zülpicher Str. 77, 50937 Köln, Germany

Version of July 22, 2022

ABSTRACT

Context. While star formation on large molecular cloud scales and on small core and disk scales has been investigated intensely over the past decades, the connection of the large-scale interstellar material with the densest small-scale cores has been a largely neglected field.
Aims. We wish to understand how the gas is fed from clouds down to cores. This covers dynamical accretion flows as well as the physical and chemical gas properties over a broad range of spatial scales.
Methods. Using the IRAM facilities NOEMA and the IRAM 30 m telescope, we mapped large areas (640 arcmin^2) of the archetypical star formation complex Cygnus X at 3.6 mm wavelengths in line and continuum emission. The data were combined and imaged together to cover all accessible spatial scales.
Results. The scope and outline of The Cygnus Allscale Survey of Chemistry and Dynamical Environments (CASCADE) as part of the Max Planck IRAM Observatory Program (MIOP) is presented. We then focus on the first observed subregion in Cygnus X, namely the DR20 star formation site, which comprises sources in a range of evolutionary stages from cold pristine gas clumps to more evolved ultracompact HII regions. The data covering cloud to cores scales at a linear spatial resolution of < 5000 au reveal several kinematic cloud components that are likely part of several large-scale flows onto the central cores. The temperature structure of the region is investigated by means of the HCN/HNC intensity ratio and compared to dust-derived temperatures. We find that the deuterated DCO^+ emission is almost exclusively located toward regions at low temperatures below 20 K. Investigating the slopes of spatial power spectra of dense gas tracer intensity distributions (HCO^+, $H^{13}CO^+$, and N_2H^+), we find comparatively flat slopes between -2.9 and -2.6, consistent with high Mach numbers and/or active star formation in DR20.
Conclusions. This MIOP large program on star formation in Cyg X provides unique new data connecting cloud with core scales. The analysis of the DR20 data presented here highlights the potential of this program to investigate in detail the different physical and chemical aspects and their interrelations from the scale of the natal molecular cloud down to the scale of accretion onto the individual protostellar cores.

Key words. Stars: formation – ISM: clouds – ISM: kinematics and dynamics – ISM: individual objects: Cygnus X – ISM: individual objects: DR20

1. Introduction

Cloud and star formation are hierarchical processes in which gas is transported from cloud scales of tens to hundreds of parsec down to sub-au scales of the inner accretion region. While the gas and dust distributions on large scales can be studied efficiently via (sub)millimeter and radio wavelength Galactic plane surveys such as the APEX Telescope Large Area Survey of the Galaxy (ATLASGAL; Schuller et al. 2009) or the Herschel infrared Galactic Plane Survey (HIGAL; Molinari et al. 2016a), the Galactic Ring survey (GRS; Jackson et al. 2006), the HI/OH/Recombination line survey of the Milky Way (THOR; Beuther et al. 2016; Wang et al. 2020), the Global view on Star formation in the Milky Way (GLOSTAR; Brunthaler et al. 2021) and many others, the small-scale structures are more typically addressed by millimeter (mm) interferometric studies of individual target regions. However, the connection of the content of whole clouds with the smallest-scale structures has been a neglected field of research. The main reason is that single-dish instruments do not resolve the relevant core scales, and mm interferometers did not allow efficient mapping of large areas on the sky so far. On their own, they cannot image extended structures.

⋆ The data are available in electronic form at the CDS via anonymous ftp to cdsarc.u-strasbg.fr (130.79.128.5) or via http://cdsweb.u-strasbg.fr/cgi-bin/qcat?J/A+A/

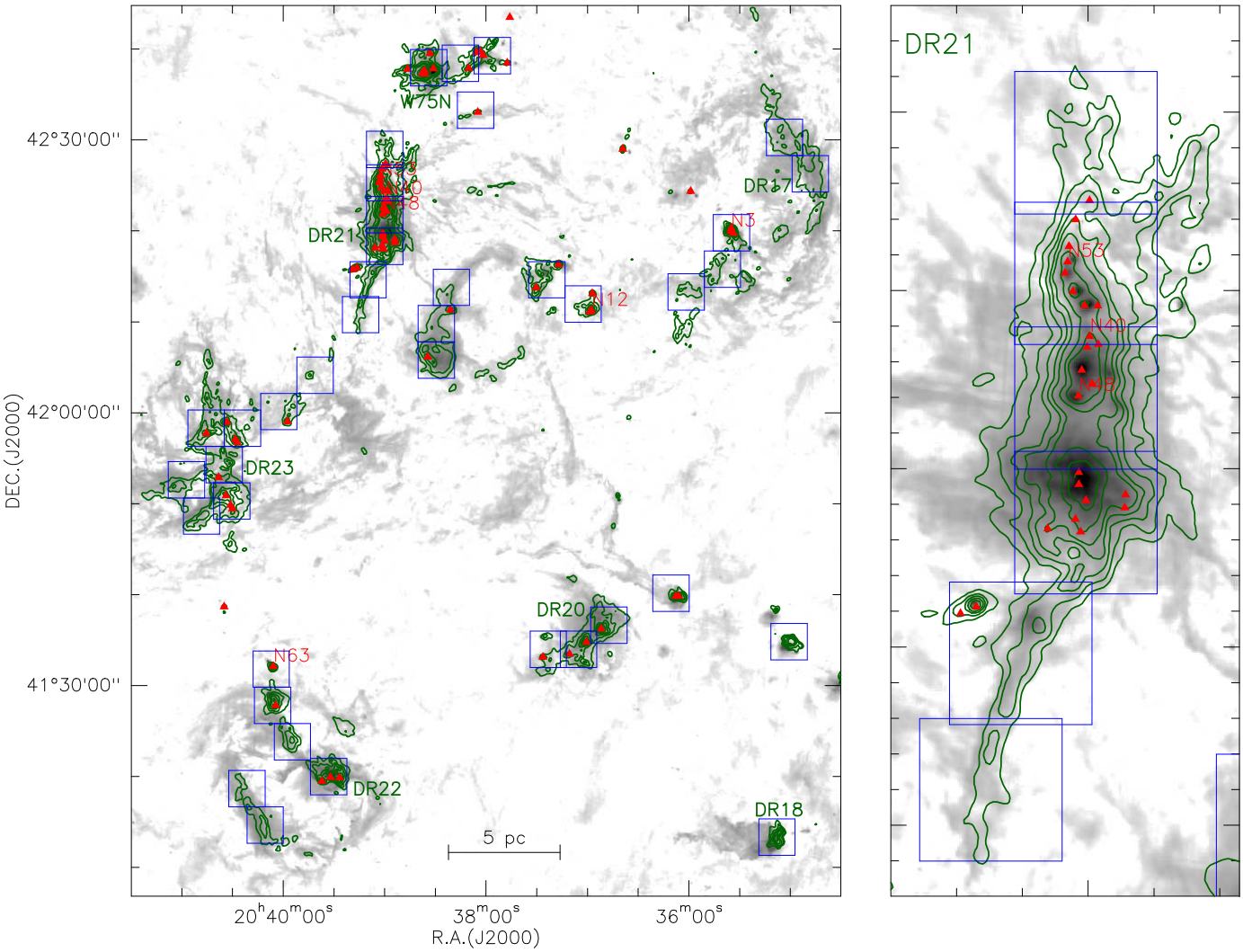

Fig. 1. Cygnus X as seen in Herschel SPIRE 250 μm (green contours) and PACS 70 μm emission (grayscale, from the HOBYS program, Motte et al. 2010). The red triangles show the mm clumps previously identified in 11″ resolution 1.1 mm single-dish mapping (Motte et al. 2007). The blue squares indicate the 16 arcmin^2 NOEMA mosaics. To the right, a zoom into the DR21 ridge is shown.

A complete picture of cloud structure and star formation can be attained by combining the capabilities of the upgraded Northern Extended Millimeter Array (NOEMA) with the IRAM 30 m telescope to trace all spatial scales. This combination allows sensitive large-scale mapping of a whole spatial resolution with a broad spectral bandpass, sensitively tracing the continuum emission and a plethora of important spectral lines. Therefore, we have set up the large Max-Planck-IRAM Observing Program (MIOP) to map the molecular cloud Cygnus X at high angular resolution with NOEMA and the IRAM 30 m telescope: The **C**ygnus **A**llscale **S**urvey of **C**hemistry **a**nd **D**ynamical **E**nvironments (CASCADE). The NOEMA part of the project is observed in ~520 h distributed over several years. Observations of the first regions started during the 2019/2020 winter semester. The complementary IRAM 30 m data were observed between May and August 2020 and will be presented with an overview of all subregions in Christensen et al. (in prep.). Furthermore, that paper will focus on the deuteration of various molecules on large cloud scales.

With the rich combined NOEMA+30 m data provided by CASCADE, we will study a broad range of scientific questions. The key topics to be addressed relate to the gas flow from large cloud scales to small core scales. We will investigate potential kinematic signatures of cloud collapse, and study how signatures may vary for different evolutionary stages. Furthermore, CASCADE will allows us to scrutinize how star-forming cores affect their environment, and which feedback processes from the newly forming stars are dominating. In addition to this, we will also study the low-mass population is such a high-mass environment. To be more specific, in the following, we outline a few topics in more detail.

Detailed studies of cloud collapse: Theoretical models differ in their predictions for the expected velocity field during the collapse phase. In the two extreme cases for fast and slow collapse (Larson 2003), much broader line profiles are expected for a runaway collapse than for quasi-static contraction (e.g., Zhou 1992). While no such broad lines are observed toward low-mass star-forming regions, the fast collapse might be relevant for high-mass star-forming cores. Models of high-mass cluster formation also predict a large-scale contraction (global collapse) as the protocluster evolves and molecular gas is funneled from the outer regions of the core into the center of the cluster (Bonnell & Bate 2002; Bonnell et al. 2004; Vázquez-Semadeni et al. 2019). The question is how these global collapse scenarios can

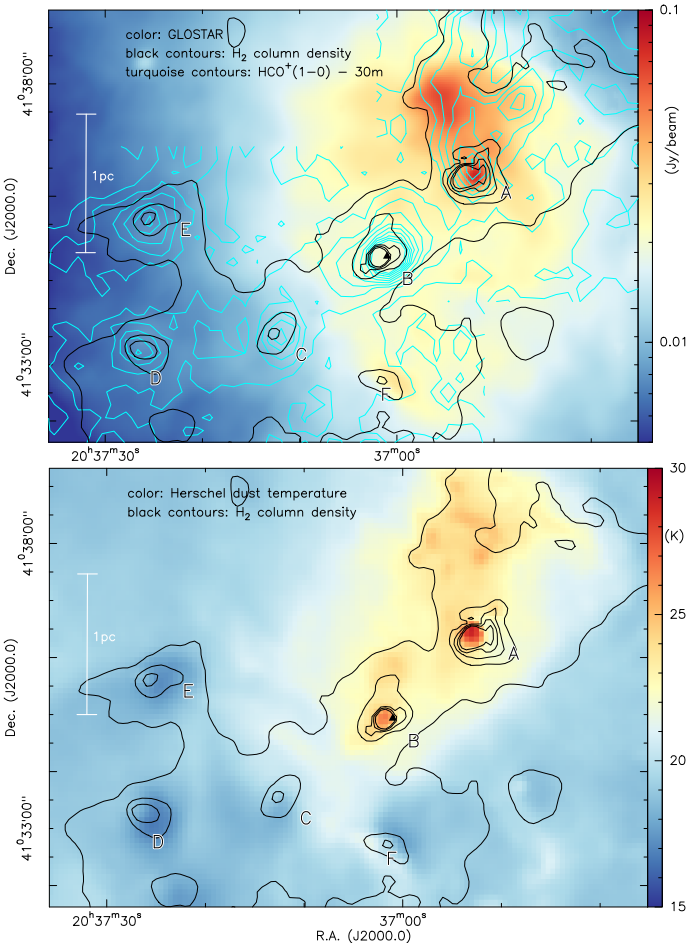

Fig. 2. Overview of the DR20 region. Top panel: Radio continuum emission from the GLOSTAR survey at 5.8 GHz with an angular resolution of 19″ is shown on the color scale (corresponding to 0.13 pc; Brunthaler et al. 2021). The turquoise contours present the $HCO^+(1-0)$ data obtained with the IRAM 30 m telescope, integrated between −7 and 3 km s^{-1}. Contour levels start at $4\sigma = 3.4$ K km s^{-1} and continue in 4σ steps. Bottom panel: Dust temperature map derived from the Herschel far-infrared continuum data by Marsh et al. (2017) is show on the color scale. In both panels, the black contours show the H_2 column density map derived by Marsh et al. (2017) at contour levels between 10^{22} and 5×10^{22} cm^{-2} (step 1×10^{22}). A linear scale-bar is shown at the left. The six main regions A to F are marked, and a triangle shows the position of the class II CH_3OH maser associated with B that has been determined by Ortiz-León et al. (2021).

be probed. Vázquez-Semadeni et al. (2009, 2019) discussed a hierarchical global collapse scenario in which the velocity dispersion on all scales was driven by global infall rather than turbulence. Observationally, indications have been found of global infall in low- (e.g., Walsh et al. 2006) and high-mass star-forming regions (e.g., Schneider et al. 2010; Beuther et al. 2020). With the MIOP project, we will be able to study the infall kinematics over a broad range of spatial scales.

Filaments: Although the existence of filamentary structures has been known for some time, Herschel studies revealed the ubiquity and importance of filaments for the cloud and star formation process (e.g., André et al. 2014). The general picture emerging from a wealth of observational and theoretical studies indicates that molecular clouds often fragment into networks of filaments, and these filaments further fragment into star-forming cores. High-mass star formation is often observed at junctions of filaments (so-called hubs; e.g., Motte et al. 2018; Kumar et al. 2020). The filaments may act as a funnel through which the gas can flow, and they link the large-scale cloud to the small-scale cores. Accretion along filaments has been found from low- to high-mass star-forming regions (e.g., Tobin et al. 2012; Kirk et al. 2013; Peretto et al. 2014; Hacar et al. 2017, 2022). The exact properties of the filaments are subject of intense debate (e.g., Arzoumanian et al. 2011; Hacar et al. 2013; Panopoulou et al. 2017; Suri et al. 2019), and it is far from clear whether filamentary structures in high- and low-mass star-forming regions behave in a self-similar way or if they vary significantly for the two regimes. The CASCADE program will allow us to address several important questions about filaments in high-mass star formation, e.g., (i) whether we see gas flow motions along filaments, (ii) whether the gas flows via a network of filaments toward the main structures, and (iii) we will be able to determine the physical properties of the massive filaments such as width, velocity dispersion, and mass-to-length ratios.

Deuterated molecules: In cold molecular clouds, deuterium enhancement, or deuteration, raises the abundance of deuterated molecules relative to their main isotopologs to values that are orders of magnitude higher than the abundance of D (relative to H) in the general interstellar medium (where it is $\sim 10^{-5}$; Oliveira et al. 2003). With the extension of the NOEMA tuning range to frequencies as low as 71 GHz, access to several ground-state transitions of important deuterated species has become available (e.g., DCN and DCO^+; Table 1). These observations will allow studies of the detailed morphology, kinematics, and deuteration fraction of the individual deuterated species from clump to core scales and lead to deuteration fractions of the different species that provide powerful constraints on models for the formation route of the deuterated species. Albertsson et al. (2013) modeled the deuteration fraction for a variety of molecules, initial conditions, timescales, and physical parameters, which our observations will be able to constrain. Körtgen et al. (2017) performed 3D magnetohydrodynamical simulations of the deuteration in massive dense prestellar cores. Interestingly, Pillai et al. (2012) found that the fundamental H_2D^+ cation in the DR21 ridge in Cygnus X does not follow the dust continuum. Therefore it is crucial to spatially resolve the emission of deuterated molecules. Here we wish to understand, for example, (i) in which density regime N_2D^+ and N_2H^+ , for instance, trace the quiescent gas, (ii) which other deuterated species behave similarly (e.g., DCO^+, DCN, or DNC), and (iii) we aim to determine the influence of the deeply embedded low-luminosity young stellar objects (YSOs) on the deuteration.

2. The nearby Cygnus X region: A star formation powerhouse

The target region for CASCADE is the well-studied northern hemisphere Cygnus X complex (e.g., Reipurth 2008, Fig. 1). This relatively nearby ($\sim$ 1.4 kpc, Rygl et al. 2012) massive and luminous region (e.g., Kumar & Grave 2007; Beerer et al. 2010) is an excellent hunting ground in which to study various phases of massive star formation. Its associated giant molecular cloud complex harbors a rich collection of objects in various star formation stages: dense, dusty, hot cores with embedded protostars (e.g., Schneider et al. 2006; Motte et al. 2007). This and the presence of several OB associations, the results of many million years of recent star formation, and a super-bubble driven by

stellar winds of the O stars and the famous Cygnus loop supernova remnant (also known as the Diamond ring) give testament to intense and widespread star formation that occurred over (at least) the past few million years. More recently, mm and centimeter (cm) wavelength observations have resulted in a wealth of data on the dust, ionized, and molecular gas emission in this region (e.g., Taylor et al. 2003; Motte et al. 2007, 2010; Molinari et al. 2010; Cao et al. 2019, 2021, 2022; Li et al. 2021; van der Walt et al. 2021). Taken together, these substantial complementary data form a rich background that now allows placing all spatial scales into context and following the gas flow from the large molecular clouds to the small cores. The Cygnus region is thus one of the few relatively nearby regions in which many phenomena can be studied in detail.

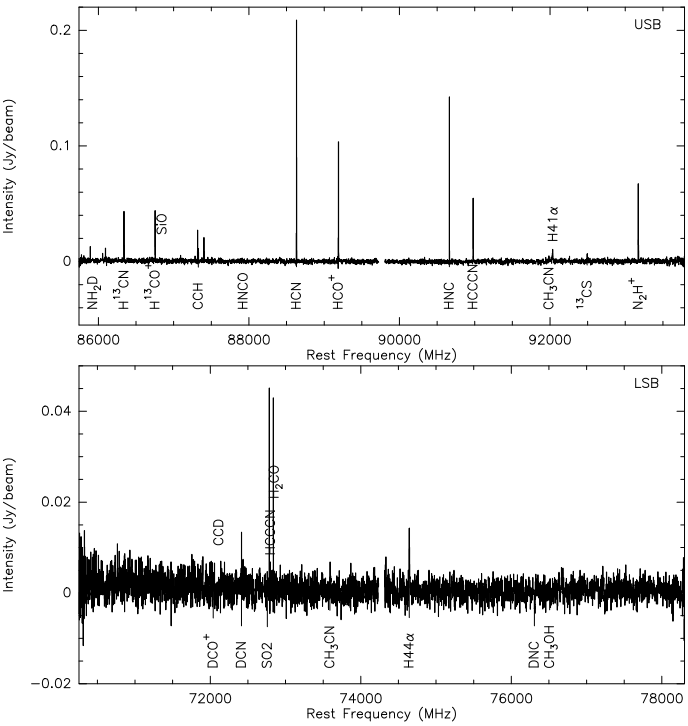

Fig. 3. NOEMA+30 m wide-band spectra toward the main continuum peak position A.

3. The Max Planck IRAM Observatory program (MIOP) on star formation in Cygnus X

Figure 1 gives an overview of the Cygnus X region observed with Herschel at the far-infrared wavelength (250 μm). While the entire complex covers several square degrees on the sky, the high-column density regions visible in the Herschel data are constrained to comparably smaller areas. The CASCADE program targets all the important subregions with 40 mosaics covering 16 arcmin^2 each (each blue square in Fig. 1 marks one mosaic). Several individual and adjacent mosaic fields are then combined into larger mosaics. For example, the prominent DR21 region shown in the right panel of Fig. 1 comprises six mosaics.

Our selected spectral setup in the 3.6 mm wavelength band of ~8 GHz width in the upper and lower sideband covers crucial ground-state lines from N_2H^+, HCN, HNC, and H_2CO, for example, as well as unique lines from deuterated molecules. Figure 3 shows example spectra taken toward the main continuum emission peak in the DR20 region with the broadband correlator unit, which has a spectral resolution of 2.0 MHz, corresponding to a velocity resolution of ~7.3 km s^{-1} at the central nominal frequency of ~82.028 GHz (Table 1). Important lines are marked. Most of these lines are also covered by additional high-resolution correlator units to also resolve them at a high spectral resolution of 60 kHz, corresponding to a velocity resolution between 0.26 and 0.19 km s^{-1} at the bottom and top end of the bandpass (Fig. 3). Table A.1 presents all spectral units, covered frequencies, and specific associated lines. These lines cover a broad range of energies above the ground state, critical densities, optical depths, and chemical properties. This allows us to probe the kinematics and the physical and chemical conditions of the dense regions on 5000 au scales in detail.

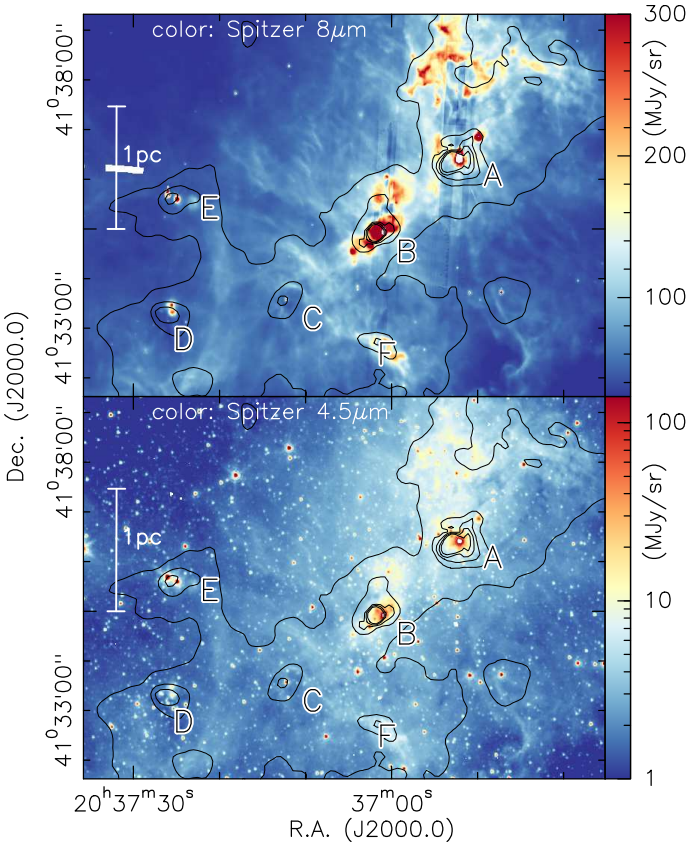

Fig. 4. Spitzer 8 μm and 4.5 μm data on the color scale. The black contours again show the H_2 column density map in contour levels between 10^{22} and 5×10^{22} cm^{-2} (step 1×10^{22} cm^{-2}).

Each individual mosaic consists of 78 pointings, and we observe all regions in the C and D configurations. This NOEMA part of CASCADE is planned to take roughly 520 h. To complement the missing short spacings, we furthermore applied for open time at the IRAM 30 m telescope. Within ~80 h of observing time, we already observed all fields with the IRAM 30 m telescope in 2020. The entire IRAM 30 m dataset is presented in a forthcoming paper by Christensen et al..

The following case study focuses on the Cygnus X subregion DR20, which was first discussed by Downes & Rinehart (1966). It is a strong radio and mm source that was investigated in various studies (e.g., Schneider et al. 2006; Motte et al. 2007) and is also part of the recent GLOSTAR Galactic plane survey (Brunthaler et al. 2021). Figure 2 shows an overview of the complex based on Herschel dust continuum and GLOSTAR radio continuum data (Marsh et al. 2017; Brunthaler et al. 2021). DR20 exhibits an almost filamentary structure from the northwest toward

the southeast, and it combines sources in a range of evolutionary stages, from more evolved (ultracompact) HII regions (clumps A and B in Fig. 2) to the younger and colder clumps C to F. This variety of evolutionary stages makes DR20 an ideal template for a first exploration of the potential of the CASCADE project.

The DR20 region, the focus of this paper, was observed with three mosaic tiles, covering star-forming regions in different evolutionary stages (Fig. 2). All NOEMA and IRAM 30 m data have been taken, and we present the full combined dataset. This allows us to also discuss the observation and data reduction challenges associated with the project.

4. Observations and data reduction

The three mosaic tiles of the DR20 region were observed individually with NOEMA in the C and D configurations between 2019 December 15 and 2020 May 3, with typically ten antennas in the array (baselines between ~15 and ~365 m). Each mosaic tile consists of 78 pointings. The phase reference centers (in J2000.0) of the three fields are R.A. 20:36:47.570 Dec. +41:36:50.40, R.A. 20:37:05.437 Dec. +41:34:10.40, and R.A. 20:37:23.303 Dec. +41:34:10.40.

The $v_{\rm LSR}$ for all three fields is the same with $-2.0\,{\rm km\,s^{-1}}$. The bandpass and flux calibration was conducted with the quasar 3C454.3 and with MWC349, respectively. Gain calibration was performed via regularly interleaved observations of the quasars 2005+403 and 2120+445.

A technical challenge of this MIOP project is achieving the desired homogeneous sensitivity distribution throughout the 40 mosaic tiles. A complete track that observes one full mosaic of 78 pointings with three coverages, which is required to reach the targeted mosaic sensitivity of ~11 mJy beam^{-1} in 150 kHz channels, takes about 9 h of telescope time. It is therefore important to protect against possibly varying weather conditions during individual tracks, and against technical failures that could unexpectedly interrupt an observing track when only part of the complete mosaic is observed. To reach this goal, a suite of dedicated observing procedures was developed that easily allow to add additional data to individual parts of the mosaic, when needed.

The calibration and imaging was performed with the CLIC and MAPPING software within the GILDAS package[1]. The continuum dataset was created using only the line-free parts of the spectrum. Excluding the band edges and the lines, we still have a very broad bandpass of ~15.51 GHz for our final continuum dataset. To create the final continuum table, we first averaged over 20 MHz bins to properly rescale the uv coordinates to the mean frequency of each bin. The UV_CONT task then created the final continuum table, taking the spectral slope of the data into account. We applied natural weighting during the imaging process for optimal imaging quality in these large mosaics. For the 3.6 mm continuum data, this resulted in synthesized beams of $3.45'' \times 2.77''$ (P.A. 21 deg), corresponding to an approximate linear spatial resolution of ~4400 au. The achieved 1σ rms noise level of the continuum data is ~50 μJy beam^{-1}. The absolute flux scale is estimated to be correct within 10%.

For the spectral line data, we obtained complementary single-dish observations with the IRAM 30 m telescope to compensate for the missing short spacings. These 30 m observations were conducted in on-the-fly mode, typically achieving rms values of ~0.1 K ($T_{\rm mb}$). The IRAM 30 m data of the entire MIOP program toward Cygnus X are presented in Christensen et al. (in prep.).

[1] http://www.iram.fr/IRAMFR/GILDAS

We then combined the NOEMA and 30 m data in the imaging process with the task UV_SHORT. All spectral line results presented in this paper are based on the combined NOEMA C+D array plus IRAM 30 m observations. Because the spectral resolution of the 30 m data is slightly lower, we used a homogeneous velocity resolution of $0.8\,{\rm km\,s^{-1}}$. Only the broad hydrogen recombination lines were imaged at a lower velocity resolution of $3\,{\rm km\,s^{-1}}$. Again, natural weighting was applied, and the final 1σ rms and synthesized beam values are presented in Table 1. The highest angular resolution is achieved for the $N_2H^+(1-0)$ line at 93.174 GHz with $3.04'' \times 2.28''$ or ~3700 au.

Table 1. Continuum and spectral line parameters.

line	freq. (GHz)	1σ $\left(\frac{\rm mJy}{\rm beam}\right)$	beam
continuum	82.028	0.05	$3.45'' \times 2.77''$
$DCO^+(1–0)$	72.039	10	$4.11'' \times 3.12''$
CCD(1–0)	72.108	10	$4.11'' \times 3.12''$
DCN(1–0)	72.415	9	$4.09'' \times 3.11''$
$SO_2(6_{0,6} - 5_{1,5})$	72.758	9	$4.07'' \times 3.09''$
HCCCN(8–7)	72.784	8	$4.07'' \times 3.09''$
$H_2CO(1_{0,1} - 0_{0,0})$	72.838	8	$4.07'' \times 3.09''$
$CH_3CN(4_k - 3_k)$	73.590	8	$4.03'' \times 3.07''$
H44α	74.645	4.5	$3.91'' \times 3.00''$
DNC(1–0)	76.306	7	$3.85'' \times 2.93''$
$CH_3OH(5_{0,5} - 4_{1,3})$E	76.510	7	$3.84'' \times 2.93''$
$NH_2D(1_{1,1} - 1_{0,1})$	85.926	6	$3.31'' \times 2.49''$
$H^{13}CN$(1–0)	86.340	7	$3.29'' \times 2.47''$
$H^{13}CO^+$(1–0)	86.754	6	$3.28'' \times 2.47''$
SiO(2–1)	86.847	6	$3.27'' \times 2.46''$
$HN^{13}C$(1–0)	87.091	7	$3.27'' \times 2.46''$
CCH(1–0)	87.329	6	$3.26'' \times 2.45''$
$HNCO(4_{0,4} - 3_{0,3})$	87.925	6	$3.23'' \times 2.44''$
HCN(1–0)	88.632	7	$3.21'' \times 2.42''$
HCO^+(1–0)	89.189	6	$3.19'' \times 2.41''$
HNC(1–0)	90.664	7	$3.13'' \times 2.33''$
HCCCN(10–9)	90.979	7	$3.12'' \times 2.32''$
$CH_3CN(5_k - 4_k)$	91.987	7	$3.08'' \times 2.30''$
H41α	92.034	4.5	$3.08'' \times 2.30''$
^{13}CS(2–1)	92.494	7	$3.06'' \times 2.29''$
N_2H^+(1–0)	93.174	8	$3.04'' \times 2.28''$

Notes: The 1σ rms values are for all lines with a resolution of $0.8\,{\rm km\,s^{-1}}$, except of the hydrogen recombination lines, which have a resolution of $3\,{\rm km\,s^{-1}}$. The continuum rms is for the whole bandpass, excluding the strong spectral lines.

5. Results

Figures 2 and 4 present overviews of the DR20 region by showing the GLOSTAR 5.8 GHz radio continuum emission (Brunthaler et al. 2021), two Spitzer mid-infrared bands (8 and 4.5 μm), and the integrated emission of the $HCO^+(1-0)$ line obtained with the IRAM 30 m telescope. Furthermore, the H_2 column densities and the dust temperatures derived by Marsh et al. (2017) from the HIGAL data (Molinari et al. 2016b) are shown. As mentioned above, a gradient in star formation activity over the region can be identified in which the western part already hosts an HII region (near A) that is shown by the radio and strong mid-infrared emission. Region B also shows elevated temperatures, strong compact molecular emission, and a class II CH_3OH maser found by Ortiz-León et al. (2021). Class

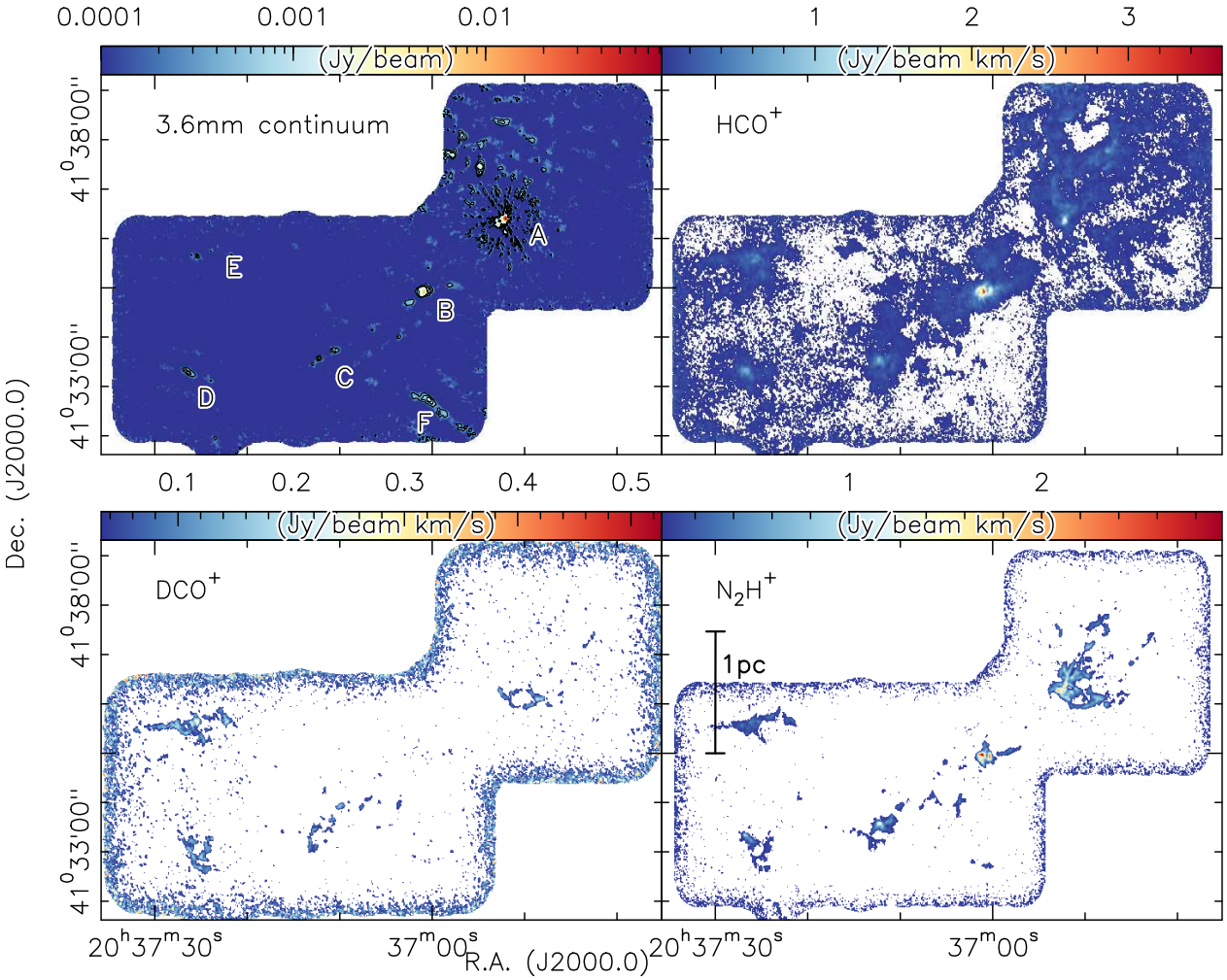

Fig. 5. Millimeter continuum and selected integrated intensity images. The upper left panel shows the 3.6 mm continuum emission (NOEMA only), and the other panels show integrated intensity images for the species marked in each panel (NOEMA+30 m). For the latter, the integration ranges are always from −7 to 3 km s^{-1}. The data were clipped below the 4σ level for each species (Table 1). The bottom right panel also shows a linear scale-bar. The six main regions A to F are labeled in the continuum panel. The continuum image also shows the lower continuum contour levels in 6σ steps of 0.3 mJy beam^{-1} up to 0.9 mJy beam^{-1}. Additional maps for other species are shown in Figures A.1 and A.2 in the appendix.

II CH_3OH masers are only found toward high-mass YSOs that are mostly in the pre-ultracompact HII region stage (Minier et al. 2003).

The eastern part is comparatively more quiescent at radio and mid-infrared wavelengths. This gradient is also reflected in the dust temperature maps in which we find elevated temperatures of about 30 K in the already active regions A and B, whereas the other four regions rather exhibit dips in the temperature map below 20 K. The $HCO^+(1-0)$ emission agrees well spatially with the general H_2 column density structure derived from the far-infrared HIGAL data. The total gas mass estimated from the H_2 column density map in the area shown in Fig. 2 is ~2500 $M_\odot$.

The different parts of the DR20 region follow an almost filamentary structure in northwest-southeast direction along four main clumps labeled A to D in Fig. 2. Adjacent to this main filament, we find two more clumps E and F, also labeled in Figure 2. The faintest clump F can barely be identified in the HCO^+ data, but is also emitting at mid-infrared wavelengths. The nearest-neighbor separations for these main clumps are about 1 pc (Table 2). Very interestingly, the classical Jeans length for a 20 K cloud at a mean density of 750 cm^{-3} is roughly 1 pc as well (e.g., Stahler & Palla 2005). A detailed analysis of the filamentary substructure and associated kinematic features will be presented in Sawczuck et al. (in prep.). That analysis will be based on a DISPERSE filament identification (Sousbie 2011; Sousbie et al. 2011) and the subsequent analysis and physical interpretation of the filamentary structures.

Table 2. Nearest-neighbor separations of the main clumps

clumps	sep. (pc)
A-B	0.88
B-C	1.11
C-D	1.08
D-E	0.96
C-F	0.97

5.1. General gas morphologies

Figure 5 and Figures A.1 and A.2 in the appendix present the 3.6 mm NOEMA-only continuum and the integrated intensity maps of the combined NOEMA+30 m line data. These images show the richness of the data obtained in this large program, which combines the capabilities of the two IRAM facilities,

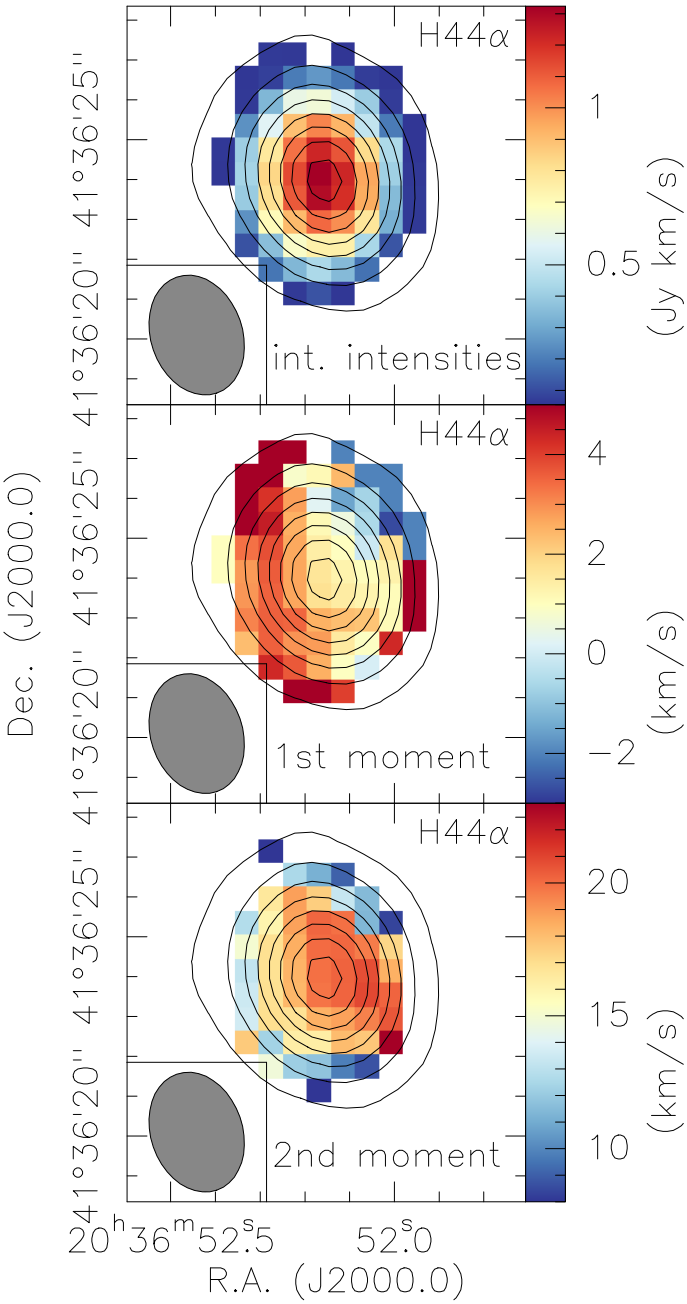

Fig. 6. Integrated intensities (top), first- (middle) and second -moment (bottom) maps of the H44α radio recombination line are shown in color scale. panel. The integration ranges are always from -20 to 20 km s^{-1}. The data were clipped below the 4σ level (Table 1). The contours show the 3.6 mm continuum data on contour levels from 8 to 78 mJy beam^{-1} (step 10 mJy beam^{-1}). The beam is shown in the bottom left corner of each panel.

NOEMA and the 30 m telescope. The continuum image still exhibits artifacts and increased noise around the strong emission sources that is caused by insufficient deconvolution because of the missing short spacings for the continuum. Except for the increased noise at the map and mosaic edges, the combined spectral line data are free from such artifacts and recover the large-scale and the small-scale emission. This allows us for the first time to study the gas properties from cloud scales down to scales of individual protostellar cores. The DR20 region is an ideal early example of the survey because it combines several aspects to be studied by this MIOP: It covers a range of evolutionary stages from an evolved HII region in the west (subregion A), close to an already ignited high-mass protostellar object whose mid-IR radiation powers a class II CH_3OH maser, to more pristine and younger regions farther east (Figs. 2 and 4). The region is observable in many spectral lines, and it harbors several structures that are connected and interacting. We discuss all these points in the following.

Because the different molecules trace different parts of the gas, our data allow us to investigate more diffuse gas components and dense components. For example, the HCO^+, HCN, or CCH emission traces more widespread and diffuse gas components, whereas other transitions,such as those from $H^{13}CO^+$ or N_2H^+ , trace the denser parts of the star-forming regions. Even denser regions can then be studied by CH_3CN or HCCCN. The emergence of deuterated species such as DCO^+, DCN, DNC, or NH_2D does not depend on density alone, but also on chemistry, and the isotopologs trace only specific parts of the gas (see section 6.2). For example, subregion F in the south of DR20 is clearly detected in the mm continuum, but only barely visible in the HCO^+ line emission. In contrast to the latter, region F is again well detected in spectral lines of H_2CO, CCH, or HNC, but it is far fainter in HCN. Hence, we identify clear differences in the chemistry throughout the entire DR20 region. Dedicated chemical investigations of the entire CASCADE data are planned as forthcoming studies.

Furthermore, we also cover two hydrogen radio recombination lines (H41α and H44α) that are typically only detected toward the strongest free-free continuum sources within a field. In the case of DR20, they are detected toward the strong cm continuum source in the west (subregion A, Fig. 2), which at the same time is also the strongest 3.6 mm source in the DR20 field (Fig. 5). Fig. 6 shows the corresponding integrated intensities and first- and second-moment maps. We return to this in section 5.3.

5.2. Core masses and column densities

The masses and column densities of the compact structures within subregions A to F can be estimated based on the 3.6 mm continuum emission (Fig. 5, top left panel). Assuming optically thin dust continuum emission at mm wavelengths, we followed the approach originally outlined in Hildebrand (1983) with the equations for gas mass and column density presented in Schuller et al. (2009) as

$$M_{\rm gas} = \frac{d^2 S_{\rm int} R}{B(T_d)\kappa_\nu} \quad (1)$$

$$N_{\rm gas} = \frac{S_{\rm peak} R}{B(T_d)\Omega\kappa_\nu \mu m_{\rm H}}, \quad (2)$$

with the distance d (1.4 kpc; Rygl et al. 2012), the integrated and peak flux densities $S_{\rm int}$ and $S_{\rm peak}$, the gas-to-dust mass ratio R (150; Draine 2011), the Planck function $B(T_d)$ depending on the dust temperature T_d, the dust absorption coefficient κ_ν, the beam size Ω, the mean molecular weight μ (~2.33; Kauffmann et al. 2008), and the mass of the hydrogen atom $m_{\rm H}$. The dust absorption coefficient κ_ν was extrapolated to 3.6 mm from Ossenkopf & Henning (1994) for dust with thin ice mantles at densities of 10^5 cm^{-3}. The dust temperatures T_d were estimated from the Herschel dust map (Fig. 2, Marsh et al. 2017). We used T_d of 29 and 27 K for regions A and B, respectively. As outlined in section 6.1 where the temperatures are estimated from

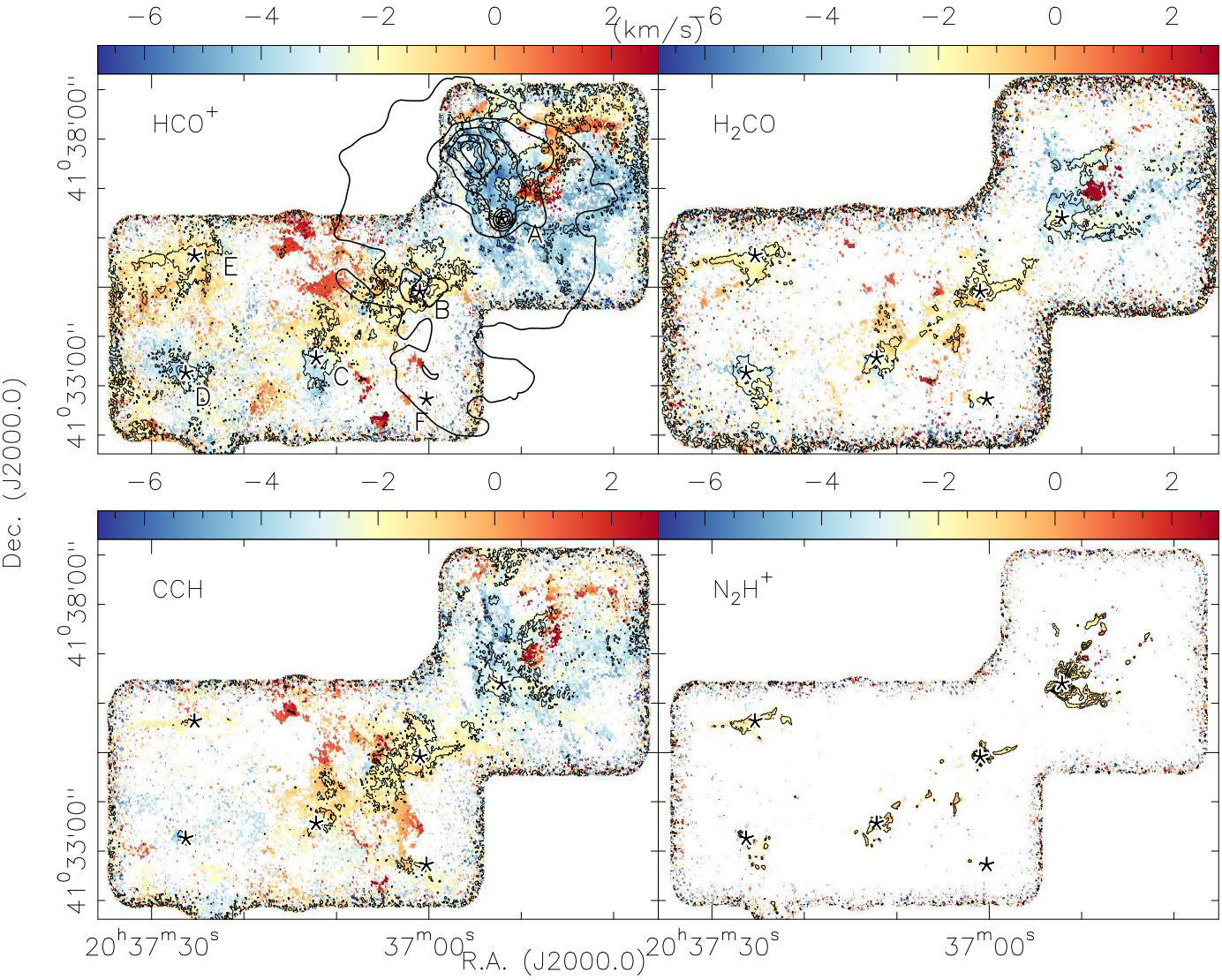

Fig. 7. First-moment maps. The colour scale always shows the first moment for the labeled species. The black contours outline the integrated emission of the same species contoured always from 0.1 to 2.9 Jy beam^{-1} km s^{-1} in steps of 0.3 Jy beam^{-1} km s^{-1}. The thick black contours in the top left panel show the GLOSTAR 5.8 GHz continuum data between 0.02 and 0.12 Jy beam^{-1} in steps of 0.01 Jy beam^{-1}. The 3.6 mm continuum peak positions are marked with five-point stars.

the HCN/HNC ratio, the temperatures derived from dust emission are likely lower limits for the more evolved regions A and B. Therefore, for comparison, we estimated the parameters for these two regions also with a higher temperature of 50 K (Table 3). For the four remaining regions, we uniformly used 20 K. The nominal 3σ point source mass and column density sensitivities for 20 K are 0.6 M$_\odot$ and 6×10^{22} cm^{-2}.

Another important information at long wavelength is how much free-free emission contributes to the measured flux densities. The GLOSTAR Galactic plane survey observed the Cygnus X region at 5.8 GHz with the Very Large Array (VLA) in two different configurations. The compact D-array observations result in the 19″ resolution image presented in Fig. 2 that shows the extended HII region encompassing our mm peak positions A and B. Estimating the free-free emission from these data in comparison to our much smaller 3.6 mm wavelength beam size of 3.45″ × 2.77″ will overestimate the free-free contribution at our wavelengths. Therefore, we also used the high-resolution B-array GLOSTAR data that have a synthesized beam of 1.5″ at 5.8 GHz. These higher-resolution data detect an almost unresolved point source toward peak A and no compact cm emission toward peak B. Using these data will hence underestimate the free-free contribution to our 3.6 mm data. To bracket the free-free contribution, we measured the 5.8 GHz flux for both datasets and extrapolated these fluxes from 5.8 GHz to 82.028 GHz assuming optically thin emission[2] via $S_{\rm free-free}(82{\rm GHz}) \sim S_{\rm free-free}(5.8{\rm GHz}) \times \left(\frac{82}{5.8}\right)^{-0.1}$. The original integrated and peak flux densities $S_{\rm int}$ and $S_{\rm peak}$ as well as the corrected values corresponding to the D- and B-array VLA observations are listed in Table 3.

Based on these assumptions and input information, the derived gas column densities $N_{\rm gas}$ and gas masses $M_{\rm gas}$ are presented in Table 3. The masses are derived within the 6σ contours around regions A to F (Fig. 5). For cores A and B, ranges are given based on the different free-free subtraction approaches and temperatures outlined above. The regions have very high

[2] At the lower frequencies close to 5.8 GHz, the optically thin assumption may not even be valid. Hence, the extrapolated free-free contributions could also be lower limits.

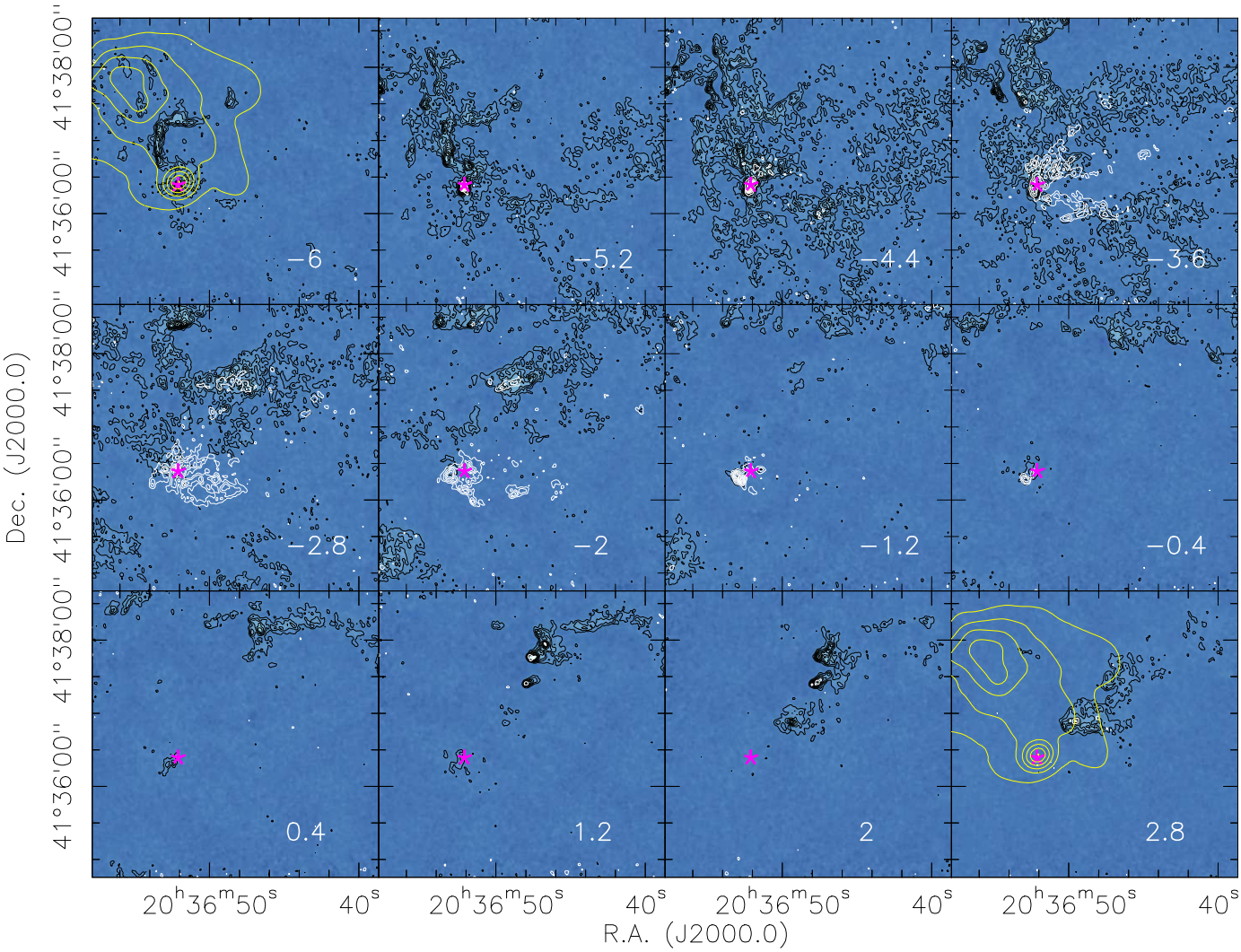

Fig. 8. Channel maps of the western third of DR20 around region A in the $HCO^+(1-0)$ and $H^{13}CO^+(1-0)$ emission lines. The colored and black contours show the $HCO^+(1-0)$ emission, whereas the white contours present the $H^{13}CO^+(1-0)$ emission. Contour levels are always in 5σ steps, and the central velocity is marked in each panel. The magenta five-point stars marks the position of the main continuum peak (Fig. 5). The yellow contours in the first and last panel outline the GLOSTAR cm continuum data from 0.03 to 0.12 Jy beam^{-1} in steps of 0.01 Jy beam^{-1}.

peak column densities between a few times 10^{23} and a few times 10^{24} cm^{-2}. The measured masses of the six main cores range between 3.8 $M_\odot$ and a potential maximum around 200 $M_\odot$ (depending on the free-free contribution and temperature, in particular, for core A). Comparing the sum of the masses shown in Table 3 with the entire mass of the region of ~2500 $M_\odot$ estimated above, we see that for the continuum data a large fraction of the flux is filtered out, since we have no continuum short spacing information in our data. Depending on the lower or upper mass ranges for cores A and B (Table 3), we recover roughly between 10 and 15% of the entire mass in our NOEMA 3.6 mm continuum data.

5.3. Gas kinematics

Figure 7 now shows the first-moment maps (intensity-weighted peak velocities) of a few specific molecules. We selected three molecules that trace the more diffuse gas (HCO^+, H_2CO, and CCH) and the dense gas (N_2H^+). Interestingly, the dense gas tracer N_2H^+ barely shows any significant velocity gradient of the large-scale DR20 region, but is mainly around -2 km s^{-1}. In contrast to this, the kinematic signatures of the other shown molecules that also trace more extended and diffuse emission are very different. While there are also large regions that have velocities around -2 km s^{-1}, we also find large areas with more blueshifted (up to -6 km s^{-1}) and more redshifted (up to $+2$ km s^{-1}) gas.

A different way to visualize these differences is a channel map. For this purpose, we selected the already shown HCO^+ and its optically thin $H^{13}CO^+$ counterpart shown in Figure 8. We focus here on the northwestern tile around main clump A that is also the most active region with an extended HII region (Figs. 2 and 4). The emission in the dense optically thin line $H^{13}CO^+$ is different from that of the main isotopolog HCO^+. More precisely, the $H^{13}CO^+$ line mainly emits in a small velocity regime around -2 km s^{-1} (Fig. 8), similar to what is seen in the first-moment map of N_2H^+ mentioned above. In comparison to this, the main isotopolog HCO^+ is rather weak in these channels, especially west of the core A peak position (magenta five-point stars in Fig. 8). While this might be self-absorption due to high-optical depth, this seems unlikely because the peak-intensities at these positions west of the core A in the optically thin $H^{13}CO^+$ line are comparably weaker than at some other positions where the HCO^+ and $H^{13}CO^+$ emissions agree spatially and spectrally much better (Figs. 8 and 9). Nevertheless, some self-absorption

Table 3. Core parameters from the 3.6 mm continuum data.

#	$S_{\rm peak}$ ($\frac{\rm mJy}{\rm beam}$)	$S^a_{\rm int}$ (mJy)	$S^b_{\rm peak-D}$ ($\frac{\rm mJy}{\rm beam}$)	$S^b_{\rm int-D}$ (mJy)	$S^c_{\rm peak-B}$ ($\frac{\rm mJy}{\rm beam}$)	$S^c_{\rm int-B}$ (mJy)	$N^g_{\rm gas}$ (10^{24}cm^{-2})	$M^g_{\rm gas}$ ($M_\odot$)	$N^g_{\rm gas}$@50K (10^{24}cm^{-2})	$M^g_{\rm gas}$@50K ($M_\odot$)
A	82.9	108.0	21.3	46.4	57.9	82.7	5.8-15.7^d	116.9-208.3^d	3.3-8.9^d	65.9-117.4^d
B	9.8	36.0	0	20.3			2.9^e	55.2-97.9^e	1.5^e	28.8-51.1^e
C^f	1.3	2.0					0.5	7.5		
D^f	1.5	4.8					0.6	18.1		
E^f	1.0	1.0					0.4	3.8		
F^f	1.1	12.0					0.5	45.2		

[a] Integrated within 6σ contours.
[b] Peak and integrated flux densities, free-free subtracted based on the GLOSTAR 5.8 GHz D-array data within the 19″ beam.
[c] Peak and integrated flux densities, free-free subtracted based on the GLOSTAR 5.8 GHz B-array integrated flux density.
[d] Column density and mass ranges based on the two free-free subtracted flux densities.
[e] Column density without free-free correction. Mass range based on D-array free-free subtracted and no free-free subtraction.
[f] no free-free contribution for these cores.
[g] $N_{\rm gas}$ and $M_{\rm gas}$ are calculated with the temperatures discussed in the text, whereas $N_{\rm gas}$ at 50K and $M_{\rm gas}$ at 50K are estimated assuming 50 K for regions A and B.

may still affect the HCO^+ emission, in particular at the highest column densities around the peak position of core A.

In contrast to $H^{13}CO^+$, the HCO^+ emission shows more extended as well as filamentary structures at more blue- and more redshifted velocity channels. In particular, the blueshifted emission between −6 and −4.4 km s^{-1} exhibits extended filamentary structures that are directly connected to the main central mm and cm continuum source. In comparison, in the redshifted channels between 1.2 and 2.8 km s^{-1} , we also identify extended and filamentary structures. These are slightly less clearly connected to the main mm and cm source in the region, but the higher the velocities, the closer the gas emission peaks to the central main source.

The spectra observed in the different parts of the region can also be studied directly. Figure 9 shows example spectra in the HCO^+(1–0) and $H^{13}CO^+$(1–0) lines toward selected positions again in the northwestern part of DR20 around clump A. Similar to the channel maps in Fig. 8, $H^{13}CO^+$ is only detected toward far fewer positions in the spectra than the main isotopolog. In the classical picture in which infall is diagnosed by asymmetric blue-skewed spectra of the optically thick species (here HCO^+) versus centrally peaked spectra of the optically thin counterpart (here $H^{13}CO^+$; e.g., Myers et al. 1996), the $H^{13}CO^+$ line is expected to peak in between the blue- and redshifted HCO^+ peaks. However, this signature is observed nowhere in the spectra of Figure 9. Therefore, the data of that region around clump A do not indicate classical global infall motions. The two velocities rather represent two different gas components in that region.

Because the blue- and redshifted molecular gas is connected via extended filamentary structures with the central star-forming core, these structures might be filamentary feeding channels in which gas might be accreted onto the central star-forming complex. Alternatively, these filaments may even be feedback signatures from the central source. We try to distinguish these two sources below.

The extended ionized gas as traced by the GLOSTAR cm continuum emission (yellow contours in Fig. 8) does exhibit emission in the northern direction that might be associated with the blueshifted gas. However, on the redshifted side, associations between the cm emission and the ionized gas appear less likely. As an additional indicator for the nature of the gas flow, the velocity dispersion may be studied, which is shown as second-moment maps (intensity-weighted velocity dispersion) in Figure 10. The velocity dispersion is largely uniformly low around 2 − 3 km s^{-1} in the northern filamentary structures at very negative velocities as well (Fig. 8). The only area with a broader velocity dispersion is the region northwest of clump A, where we had previously identified the two velocity components. Hence, the higher values in the second-moment map there do not indicate broader line widths; this is just mimicked by the two velocity components. In the framework of the above question whether the two velocity components may be caused by infall or by feedback, feedback would in general cause shocks and broader lines. Therefore, the on average narrow line widths are indicative that the two velocity components may indeed rather belong to pristine gas streamers that may be associated with the cloud and star formation processes. However, as we show in the following section 6.1, the high-velocity gas components are spatially associated with enhanced temperatures. Hence, expansion and feedback from the HII region into the pristine environmental gas may be a viable scenario to explain the high-velocity gas.

For comparison, Figure 6 also presents the first- and second-moment maps of the H44α emission toward the strongest continuum source A. Because of the lower sensitivity to the recombination line emission at mm wavelengths, the line is only detected over an extent of a few beams around the main source A. While the second-moment map typically shows broad almost thermal velocity dispersion values around 20 km s^{-1}, the first-moment map in the middle panel of Figure 6 depicts a velocity gradient in the northwest-southeast direction. In comparison, we do not identify a clear bipolar molecular outflow structure in the SiO emission. Interestingly, the blueshifted emission is toward the northwest, opposite to the redshifted molecular filaments northeast of region A that were discussed in the previous paragraphs.

6. Discussion

6.1. Gas temperatures

The temperatures of the gas provide important physical information for a general understanding of the region. While the Herschel data provide us with a dust temperature map at 12″ resolution (Fig. 2; Marsh et al. 2017), we would like to derive a temperature map at higher angular resolution from the gas lines that we have observed. Although our setup comprises a few molecules with several lines that may be used as temperature indicator, for example, from CH_3CN or CH_3OH, emission of these molecules

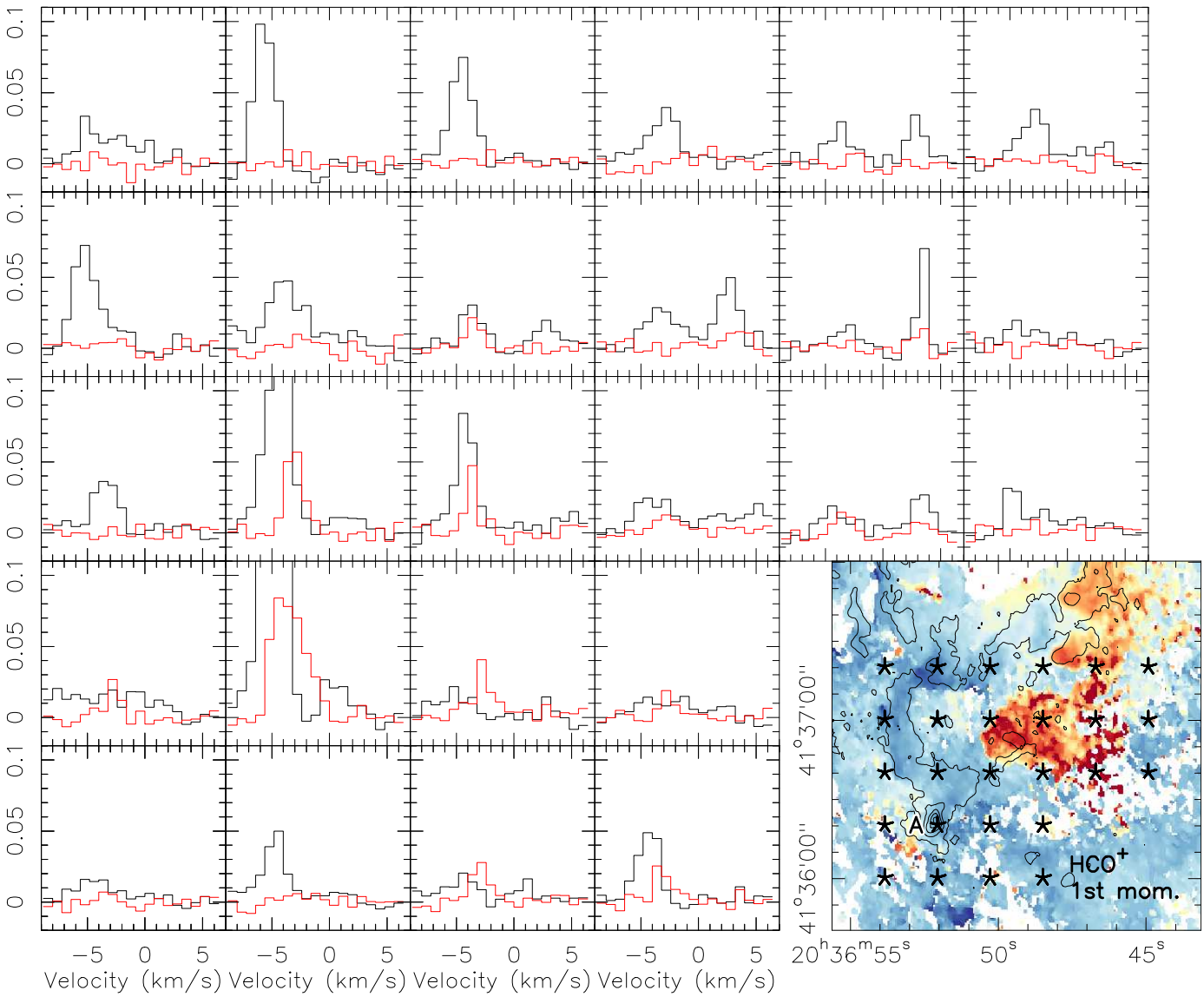

Fig. 9. $HCO^+(1-0)$ and $H^{13}CO^+(1-0)$ spectra in black and red, respectively, toward the northwestern region A of DR20. The y-axis of the spectra shows the flux densities in units of Jy beam^{-1}. The color-scale in the bottom right panel shows the corresponding HCO^+ first-moment map, in which the stars mark the positions of the presented spectra. The contours show the $HCO^+(1-0)$ integrated intensity map (from -7 to 3 km s^{-1}) from 5 to 95% of the peak emission in steps of 10%.

is typically not that widespread, but is more confined to the central densest regions. This is also the case in DR20; see Figure A.2. However, Hacar et al. (2020) recently suggested that the ratio of the HCN(1–0) and HNC(1–0) lines might be a good temperature measure, in particular in the regime between 15 and 40 K. Using the integrated intensity images shown in Fig. A.1, we created a ratio map of the two and converted this into temperatures following the recipe outlined in Hacar et al. (2020),

$$T = 10 \times \left[\frac{I(\mathrm{HCN})}{I(\mathrm{HNC})}\right] \quad \text{if} \quad \frac{I(\mathrm{HCN})}{I(\mathrm{HNC})} \leq 4 \tag{3}$$

$$T = 3 \times \left[\frac{I(\mathrm{HCN})}{I(\mathrm{HNC})} - 4\right] + 40 \quad \text{if} \quad \frac{I(\mathrm{HCN})}{I(\mathrm{HNC})} > 4. \tag{4}$$

The resulting temperature map is presented in Fig. 11. Hacar et al. (2020) estimated the uncertainties of the estimated temperatures for $10 < T < 40$ K to be $\Delta T \approx 5$ K, and above $T > 40$ K to be $\Delta T \approx 10$ K. A few general features can be pointed out in the DR20 region: In the more quiescent regions C to F, the gas temperatures are typically low, about 20 K or even lower. In contrast to this, in regions of strong cm continuum emission, as outlined by the GLOSTAR contours in Fig. 11, the temperatures rise to values above 40 K. This is particularly prominent north of region A, as well as around region B. The GLOSTAR cm continuum and Spitzer mid-infrared images in Figs. 2 and 4 conversely show that the regions of elevated temperature in the HCN/HNC temperature spatially coincide with regions of strong cm continuum and mid-infrared emission, which means ongoing or even past star formation events. This star formation can excite the environmental gas and hence explain the higher temperatures in the HCN/HNC temperature maps in these regions.

In addition to this, when the temperature map is compared to the HCO^+ channel maps (Fig. 8), the warm regions north of clump A appear to be associated with specific velocity components. To examine this in more detail, Fig. 12 presents a zoom of the temperature map toward the north-western part of DR20 around clump A. We overplot the contours of specific HCO^+ and

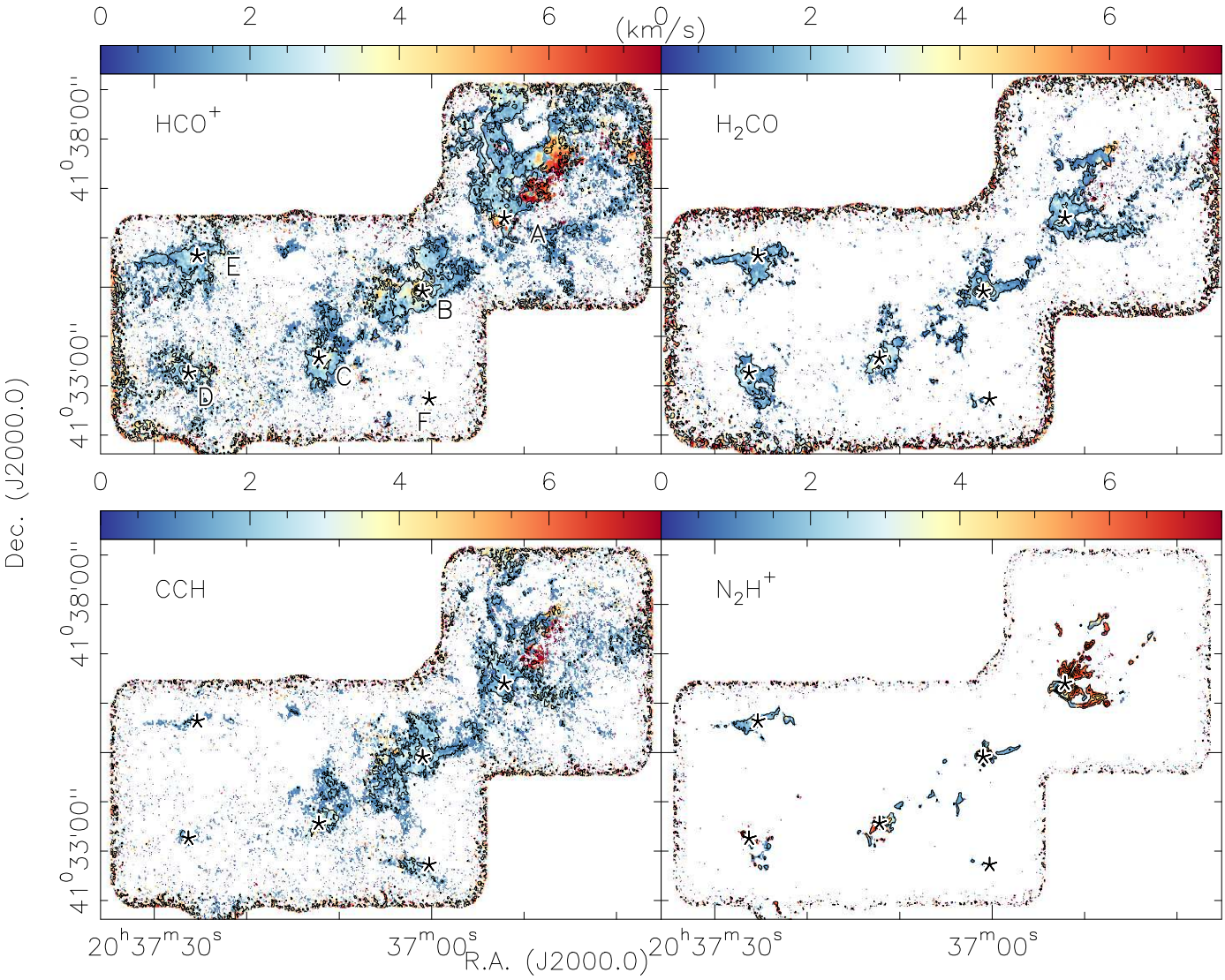

Fig. 10. Second-moment maps: The color scale always shows the second-moment for the labeled species. The black contours outline the integrated emission of the same species, always contoured from 0.1 to 2.9 Jy beam^{-1} km s^{-1} in steps of 0.3 Jy beam^{-1} km s^{-1}. The 3.6 mm continuum peak positions are marked with five-point stars.

$H^{13}CO^+$ channel and find clear associations, especially of elevated temperatures with high-velocity HCO^+ gas. The full black contours in Fig. 12 show that the blueshifted filamentary HCO^+ emission at -6 km s^{-1} is clearly associated with the warm gas north of clump A. Similarly, the redshifted gas at $+2.8$ km s^{-1} is spatially correlated with the warm gas northwest of clump A (dotted contours in Fig. 12). In contrast to this, the main dense gas structure visible in the $H^{13}CO^+$ emission at -2.8 km s^{-1} is spatially correlated with the cold gas (magenta contours in Fig. 12). Since clump A drives an expanding HII region that is visible in the cm continuum data (e.g., yellow contours in Fig. 8), a plausible interpretation for the spatial correlation between high temperatures and high-velocity gas could be that the expanding HII region heats up the gas and at the same time pushes the remnant structures of the envelope to higher velocities. In contrast to this, the higher-density tracer $H^{13}CO^+$ may trace the parts of the envelope that are still less affected by the expanding HII region.

Toward the peak positions of regions A and B, we find elevated temperatures, as expected, but especially toward B, they are slightly below the environmental higher temperatures. This is partly in contrast to the temperature map derived from the far-infrared continuum data (Fig. 2; Marsh et al. 2017) where the highest temperatures are found toward the peak positions A and B. We point out that although elevated above 20 K, the absolute values of the Herschel temperature map even in the warm regions north of region A are lower than the HCN/HNC derived values. This can be explained by the combined effect of the lower angular resolution of the Herschel data and the fact that the Herschel far-infrared wavelengths between 70 and 500 μm are not a good tracer of gas warmer than 40 K. Nevertheless, the gradients and temperature trends in the Herschel map reflect the large-scale temperature structure of the region well. Therefore, the estimated lower temperatures toward the A and B peak positions in the HCN/HNC derived temperature compared to the surroundings of A and B are most likely an artifact because toward these positions, the H_2 column densities rise above values of 10^{23} cm^{-2} (section 5.2), and the HCN and HNC emission becomes optically thick. In this regime, the ratio of the two lines decreases again and saturates at values corresponding to lower temperatures. Hacar et al. (2020) argued that up to extinctions $A_v \approx 100$, corresponding to H_2 column densities of $\sim 1 \times 10^{23}$ cm^{-2}, the HCN/HNC ratio could still be a reasonable

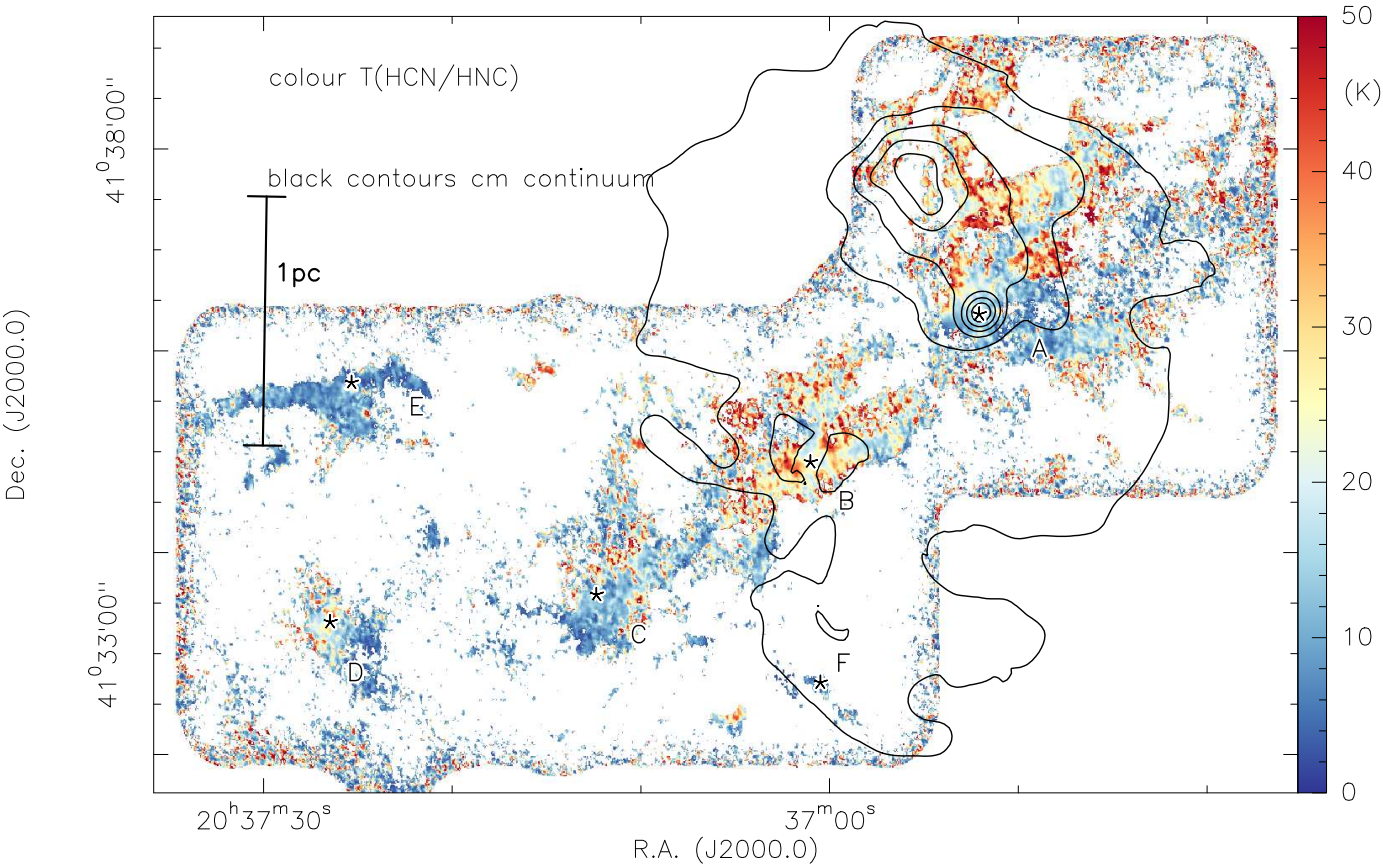

Fig. 11. Temperature map from the HCN/HNC ratio. The color-scale shows the temperature map derived from the integrated intensity ratios of the HCN(1–0) and HNC(1–0) line following Hacar et al. (2020). The black contours show the GLOSTAR cm continuum emission from 20 to 100 mJy beam^{-1} in steps of 10 mJy beam^{-1}. The 3.6 mm continuum positions are marked as five-point stars. A linear scale-bar is shown at the left, and the six main regions A to F are labeled.

column density tracer. However, toward the peak positions of A and B, we are even above that threshold (Table 3). We return to these high-column density regions below by investigating the $H^{13}CN/HN^{13}C$ ratio.

For a direct comparison of the temperature map derived from the Herschel far-infrared data (Fig. 2, Marsh et al. 2017) and our higher-resolution HCN/HNC temperature map, we smoothed the HCN/HNC temperature map to the spatial resolution of 12″ of the dust temperature map and placed them on the same grid. The ratio of these two maps is presented in Fig. 13 (top panel). It is encouraging to see that over large areas of the map, the ratio of dust temperature and HCN/HNC temperature is close to 1. This is particularly clear north of region A, in almost the entire region B, and in large parts of C and D. Excluding some edges around C and D, the only exceptions of a ratio on the order of unity are the peak of region A, some area slightly west of A, and almost the entire region E. While the difference toward the peak of A can most likely be explained by the high column densities toward that position and the accordingly increased optical depth in the HCN and HNC lines, this seems less likely to be the case for the high ratios west of A and in E.

Qualitatively speaking the dust temperature and HCN/HNC temperature maps in region E largely agree in the sense that low temperatures are found in both of them. Nevertheless, quantitatively, the estimates differ in the dust temperature map toward E, the temperatures drop below 20 K but never lower than 17 K. In contrast, the HCN/HNC temperature map there exhibits largely temperatures around 10 K or even below, implied by ratios of about 2. A similar situation can be found east of region A, where the dust temperature map ranges around 22 K, and the HCN/HNC temperature map again shows values in the 10 K regime. The higher-than-1 ratio between the dust and HCN/HNC temperatures west of peak A can be explained by the radiation in the HII region. This radiation may excite outer layers of the dust environment, and by this, increase the average line-of-sight dust temperature. In contrast, these warmer layers may not be associated with higher-density gas traced by HCN/HNC. These molecular lines rather trace the denser and cooler gas, explaining the higher ratios seen west of A in Fig. 13.

The PPMAP approach (point process map) by Marsh et al. (2015, 2017) for estimating column densities and temperatures from Herschel data has not only been applied to the integrated H_2 column density map and the line-of-sight averaged temperature maps, but also provides H_2 column density maps for different temperatures (12 bins between 8 and 50 K). The three bottom panels of Fig. 13 now show these H_2 column densities at three selected temperatures of 9.5, 18.4, and 30.3 K. The differences between these maps is large in that sources E and F are mainly found to have very low temperatures, whereas A and B have high temperatures. In source E, the dense central region receives strong contributions of cold gas and dust. However, in the line-of-sight averaged temperature map (Fig. 2), the outer warmer layers of the region contribute so strongly that temperatures below 17 K cannot be attained. In contrast to this, HCN and HNC have critical densities above 10^5 cm^{-3} and even effective excitation densities above 10^3 cm^{-3} (Shirley 2015). Hence,

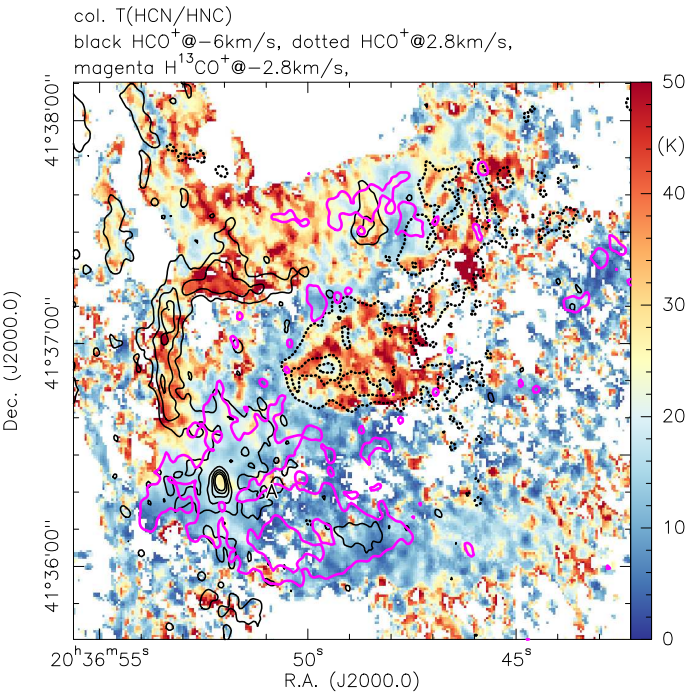

Fig. 12. Zoom of the temperature map for the northwestern area around clump A. The color-scale again shows the temperature map derived from the integrated intensity ratios of the HCN(1–0) and HNC(1–0) line following Hacar et al. (2020). The contours outline HCO^+ and $H^{13}CO^+$ emission structures at specific velocities (Fig. 8). Full black contours plot HCO^+at -6km s^{-1}, dotted contours show HCO^+at 2.8km s^{-1}, and magenta contours show $H^{13}CO^+$at -2.8km s^{-1}. Contour levels for HCO^+ start at 5σ and continue in 10σ steps. For $H^{13}CO^+$ only the 5σ contour of the 6 mJy beam^{-1} is shown.

these lines preferentially trace the higher density, and in region E, also colder gas. Therefore, measuring lower temperatures via the HCN/HNC ratio is plausible.

We return to the potential high optical depth, especially toward the peak positions A and B. We can also explore the emission from the rarer isotopologs $H^{13}CN$ and $HN^{13}C$. As shown in Fig. A.1, these rarer isotopologs are mainly detected toward the two main peak regions A and B. This is sufficient, however, because these regions also have the highest optical depth, where the main isotopologs discussed before are most prone to saturation and hence deliver temperature estimates with high uncertainties. We now applied exactly the same procedure to the integrated intensity ratio maps of $H^{13}CN$ and $HN^{13}C$ and derived a new temperature map in particular towards regions A and B. The resulting temperature distribution is shown in Fig. 14 (top panel). As expected, the highest temperatures are now found toward the peak positions of A, where the most luminous embedded sources should be located. Hence qualitatively speaking, using the rarer ^{13}C isotopologs appears to be a reasonable option to estimate temperatures toward high column density regions as well.

As a final test, we combined the results obtained with the main isotopolog lines HCN/HNC with those from their rarer ^{13}C replacements $H^{13}CN/HN^{13}C$. Assuming that the chemical behavior of the ^{12}C and the ^{13}C isotopologs is similar, we used the $H^{13}CN/HN^{13}C$ ratio where detectable and the HCN/HNC ratio for the remaining parts of the map. The result of this brute-force combination is presented in Fig. 14 (bottom panel). Interestingly, the transition between the two temperature derivations is barely recognizable in this combined map. This can be considered as an indicator that deriving the temperature distribution by this combined approach can be reasonable. While the $H^{13}CN/HN^{13}C$ ratio can be used for the highest column density regions, the HCN/HNC ratio can be employed for the remaining ga,s as introduced by Hacar et al. (2020).

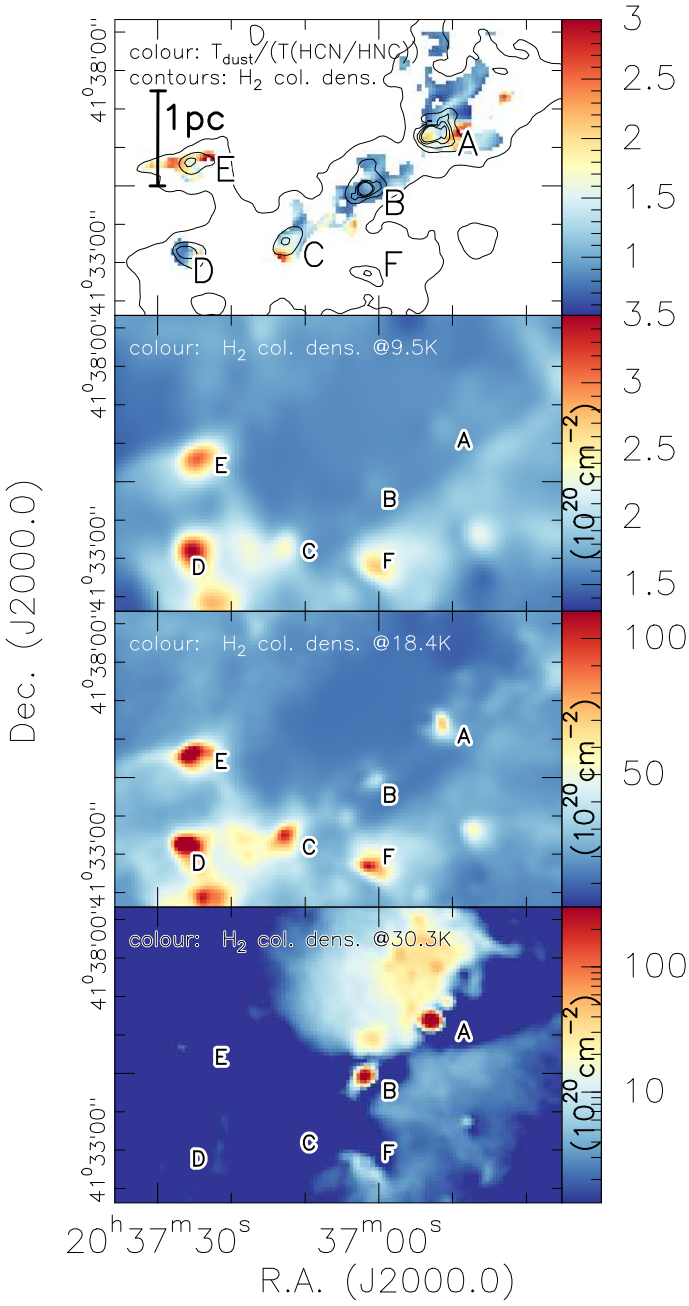

Fig. 13. Temperature ratio map and column density maps at different temperatures. *Top panel:* Ratio map of the temperatures derived from the Herschel far-infrared data (Fig. 2; Marsh et al. 2017) vs the temperature map obtained from the HCN/HNC ratio (Fig. 11; top panel). For this ratio map, the HCN and HNC data were first smoothed to the 12″ resolution of the dust temperature map. The black contours show the H_2 column density map derived by Marsh et al. (2017) at contour levels between 10^{22} and 5×10^{22} cm^{-2} (step 1×10^{22} cm^{-2}). A linear scale-bar is shown to the left. The *bottom three panels* show the H_2 column densities derived at different temperatures (as marked in the panels) as outlined in Marsh et al. (2017). The six main regions A to F are marked in all panels.

We are aware that we do not present an in-depth analysis of the chemical background of this potential thermometer as

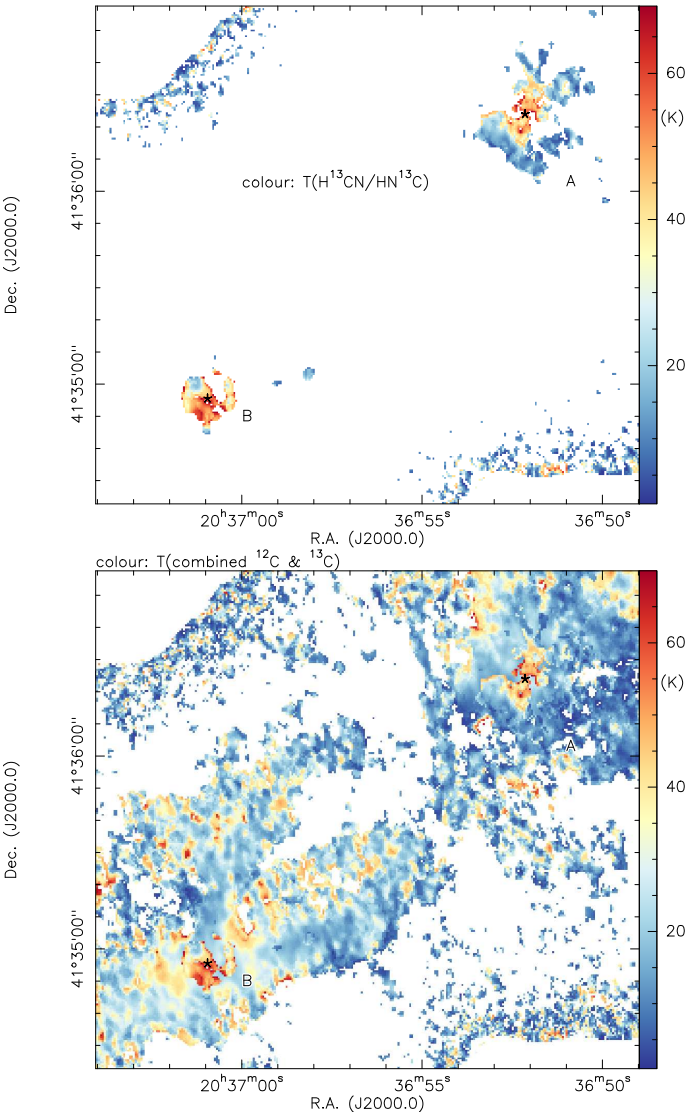

Fig. 14. Temperature maps using also the $H^{13}CN/HN^{13}C$ ratio. *Top panel:* Temperature map derived from the integrated intensity ratios of the $H^{13}CN(1–0)$ and $HN^{13}C(1–0)$ line following the procedure outlined in Hacar et al. (2020) for the main isotopologs. The five-point stars mark the 3.6 mm continuum peak positions of region A and B. The *bottom panel* presents the corresponding temperature map where the temperatures derived from HCN/HNC and $H^{13}CN/HN^{13}C$ are combined (see main text for procedure).

well. Our aim was to further explore the possibilities of using the HCN/HNC and $H^{13}CN/HN^{13}C$ ratios as gas thermometer in the 3 mm wavelength band.

6.2. Deuteration

With our spectral setup, we also cover several lines from deuterium substitute isotopologs, in particular from DCO^+, DCN, DNC, and NH_2D (Table 1). The integrated emission maps of these species presented in Figures 5, A.1, and A.2 show that in the DR20 region, the $DCO^+(1-0)$ emission is strongest and most extended. To highlight some of the questions that can be addressed with deuterated molecules, we therefore focus on the $DCO^+(1-0)$ emission. It has also been shown in the framework of the IRAM CORE large program that DCO^+ is an excellent tracer of the dynamics of the gas in very young star-forming regions (Beuther et al. 2021; Gieser et al. 2022). Because the DR20 region contains sources in several evolutionary stages, it can provide the ideal laboratory for testing whether DCO^+ indeed only traces early evolutionary stages or if more evolved regions can also be reasonably well studied by this species.

Figure 15 shows an overlay of the integrated DCO^+ emission in comparison with its non-deuterated counterpart $H^{13}CO^+$ (which we used instead of HCO^+ because of its lower abundance and hence lower optical depth). While there is a clear correlation between the distributions of the deuterated and nondeuterated species for the main cores C, D, and E, the correlation is less clear for the two more evolved regions A and B (F is too weak to be clearly detected in any of the two tracers). While DCO^+ remains entirely undetected toward region B, toward region A, it is at least detected at the southern boundary of the region, offset from the main 3.6 mm continuum emission. It is interesting to note that also towards regions C and D, the DCO^+ emission is found to be offset from the main 3.6 mm continuum peak positions. Only toward region E are $H^{13}CO^+$, DCO^+ and 3.6 mm continuum emission relatively well correlated spatially (Fig. 15). While the anticorrelation of DCO^+ with most of the continuum peaks is likely associated with high temperatures in these regions (see below), the nondetection of extended 3.6 mm continuum emission in regions of strong DCO^+ emission may also be related to the fact that in contrast to the spectral line data, where we combined NOEMA and 30 m data, we lack the complementary short spacing data for the 3.6 mm continuum and hence cannot recover extended emission.

One physical way to interpret these results is based on a comparison with the gas and dust temperature maps presented in Figures 11 and 2. Regions C, D, and E clearly have the lowest temperatures in the two temperature maps. Even the deuterated emission in the vicinity of peak A lies south and southwest of the strong mm and cm continuum emission where the gas temperatures are below 20 K. Hence, a temperature regime below 20 K clearly seems conducive for detecting deuterated DCO^+ emission. This is in line with other DCO^+ observations and modeling, for example, in the Horsehead nebula (Pety et al. 2007) or even in the Orion bar, where the deuteration in DCO^+ is comparably low at the higher temperatures in this photon-dominated region (Parise et al. 2009). The fact that the continuum peak E is associated with DCO^+ emission implies that this region is cold and has high gas column densities.

6.3. Spatial power spectra of the intensity distributions of the dense gas tracer

Power spectra of integrated intensity emission or entire spectral data cubes are used to infer the turbulent and gravitational properties of the gas in the ISM and associated with star formation (e.g., von Weizsäcker 1951; Lazarian & Pogosyan 2000; Elmegreen & Scalo 2004; Falceta-Gonçalves et al. 2015; Burkhart et al. 2010; Burkhart 2021). The power spectrum of incompressible turbulence follows a power law of $-11/3$ (Kolmogorov 1941) that can be recovered by observations of an optically thin tracer of the turbulent gas like HI (e.g., Lazarian & Pogosyan 2000; Lazarian et al. 2002; Stanimirović & Lazarian 2001; Miville-Deschênes et al. 2003; Burkhart et al. 2013). Optical depth effects can saturate this slope at -3 (e.g., Lazarian & Pogosyan 2004; Burkhart et al. 2013). Other effects can flatten this slope, and Burkhart et al. (2010) showed that the slope of the power spectrum becomes shallower for increasing Mach number because stronger turbulence creates more density irregularities and hence more energy on smaller scales (see also Hennebelle

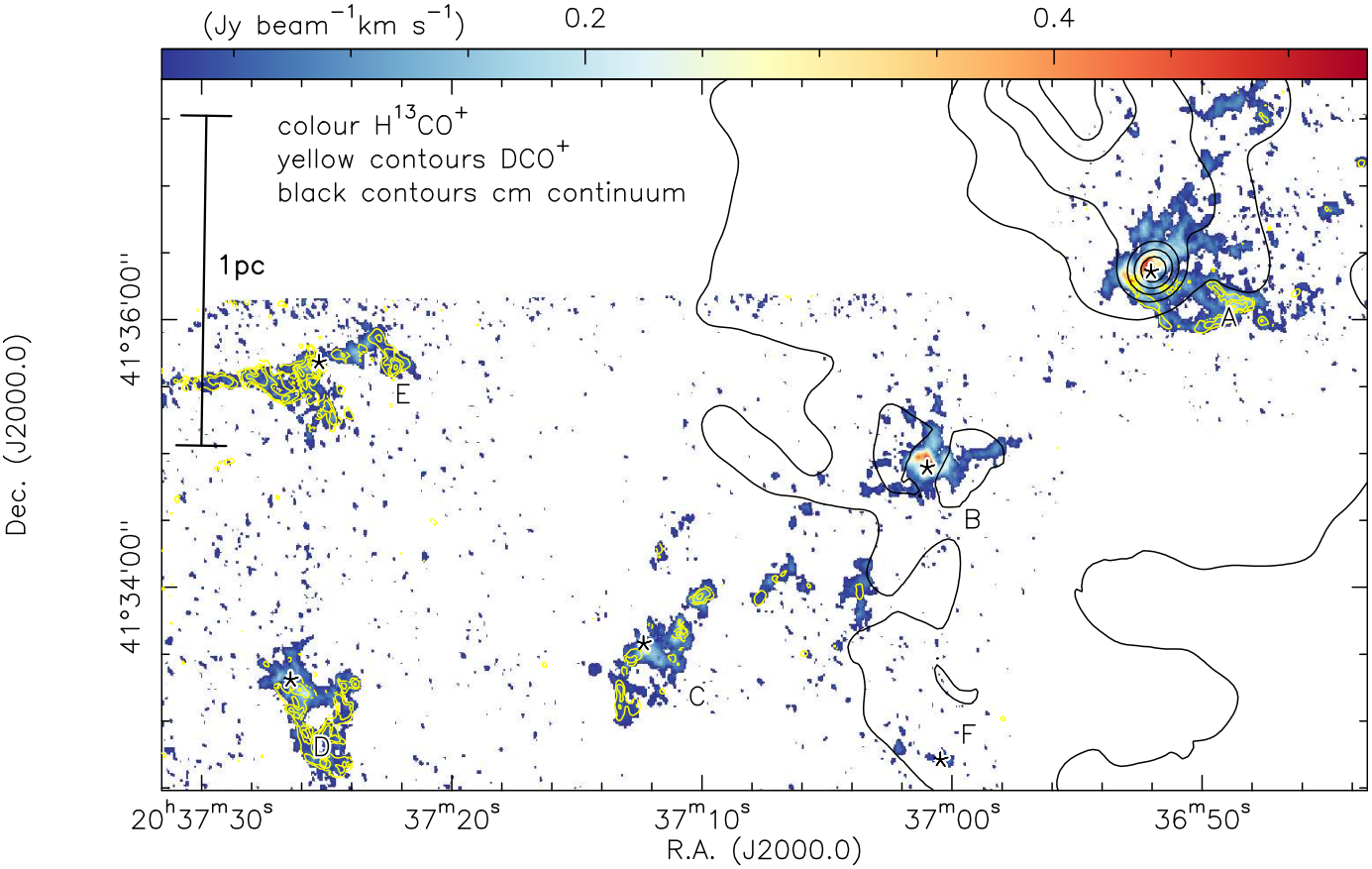

Fig. 15. Integrated $DCO^+(1-0)$ contours in yellow on $H^{13}CO^+(1-0)$ emission in color. The integration regimes for the two molecular transitions are from -7 to 3 km s^{-1}. The yellow DCO^+ contours are from 50 to 500 mJy beam^{-1}km s^{-1} in steps of 50 mJy beam^{-1}km s^{-1}. The black contours show the GLOSTAR cm continuum emission from 20 to 100 mJy beam^{-1} in steps of 10 mJy beam^{-1}. A linear scale-bar is shown to the left, and the six main regions A to F are labeled and marked by five-point stars.

& Falgarone 2012). In addition to this, self-gravity flattens the slopes of the power spectra even more (e.g., Collins et al. 2012; Federrath & Klessen 2013; Burkhart et al. 2015). This latter picture was recently observationally confirmed by multitracer observations and analysis of the Perseus molecular cloud: Pingel et al. (2018) investigated the power spectra of HI, ^{12}CO, ^{13}CO, and dust data of the Perseus cloud and reported power-law slopes of −3.2, −3.1,− 2.9, and −2.7 for the four tracers, respectively. Hence, tracers of increasing density typically associated with increasing star formation activity exhibit increasingly shallower power-law slopes.

This latter scenario can now be investigated further with our MIOP observations in Cygnus X. While at our high angular resolution we lack data for the complementary low-column density tracers such as HI or CO, we observe a broad range of higher-density gas tracers. In the following, we concentrate on the optically thick and thin pair of $HCO^+(1-0)/H^{13}CO^+(1-0)$ and on the $N_2H^+(1-0)$ line emission. While all three lines have critical densities of about 4×10^4 cm^3, their effective excitation densities at 20 K span a broader range with 5.3×10^2 cm^3, 2.2×10^4 cm^3, and 5.5×10^3 cm^3, respectively (Shirley 2015). Hence, all lines trace dense gas in which star formation activity and correspondingly gravity are expected to dominate.

To extract the slopes of the power spectra for these three tracers for the entire DR20 region mapped here, we used the python package TurbuStat (Koch et al. 2019). To avoid any artifacts caused by noise, we used the images presented in Figures 5 and A.1 with the modification that we increased the threshold for creating the integrated intensity maps to 5σ, and we masked the edges of the mosaics where the noise increases again. For HCO^+ and $H^{13}CO^+$, we used the standard integration range from −7 to +3 km s^{-1}. For N_2H^+ we increased the integration range to −12 to +6 km s^{-1} to cover the entire hyperfine structure. We derived the power spectra over spatial scales between 5″ (larger than the angular resolution) and 90″, roughly the largest size-scale that can be identified in the N_2H^+ and $H^{13}CO^+$ data (Figs. 5 and A.1). The derived power-law slopes are from 1D fits to the azimuthally averaged 2D power spectra. With this approach, we obtain power-law slopes of the power spectra for HCO^+, $H^{13}CO^+$, and N_2H^+ of −2.9, −2.7, and −2.6, respectively (Fig. 16). The standard deviation of the fits to the slopes in all three cases is smaller than 0.1.

These estimates in context with the power spectra results reported in the literature and introduced above show that the high optical depth and comparably lower density tracer HCO^+ with −2.9 shows a power-law slope that is close to the saturated −3.0 value discussed by Lazarian & Pogosyan (2004) and Burkhart et al. (2013). In comparison to this, the two higher-density tracers $H^{13}CO^+$ and N_2H^+ reveal consistently flatter slopes of −2.7 and −2.6 that are expected for increased Mach numbers and/or self-gravity becoming dominant compared to the initially more turbulent gas where the slopes are steeper (e.g., Burkhart et al. 2010, 2015; Collins et al. 2012; Federrath & Klessen 2013). The slopes found here for the dense gas tracers are also comparable to those found in other studies based on dust extinction and emission, which also trace the densest parts of the star-forming

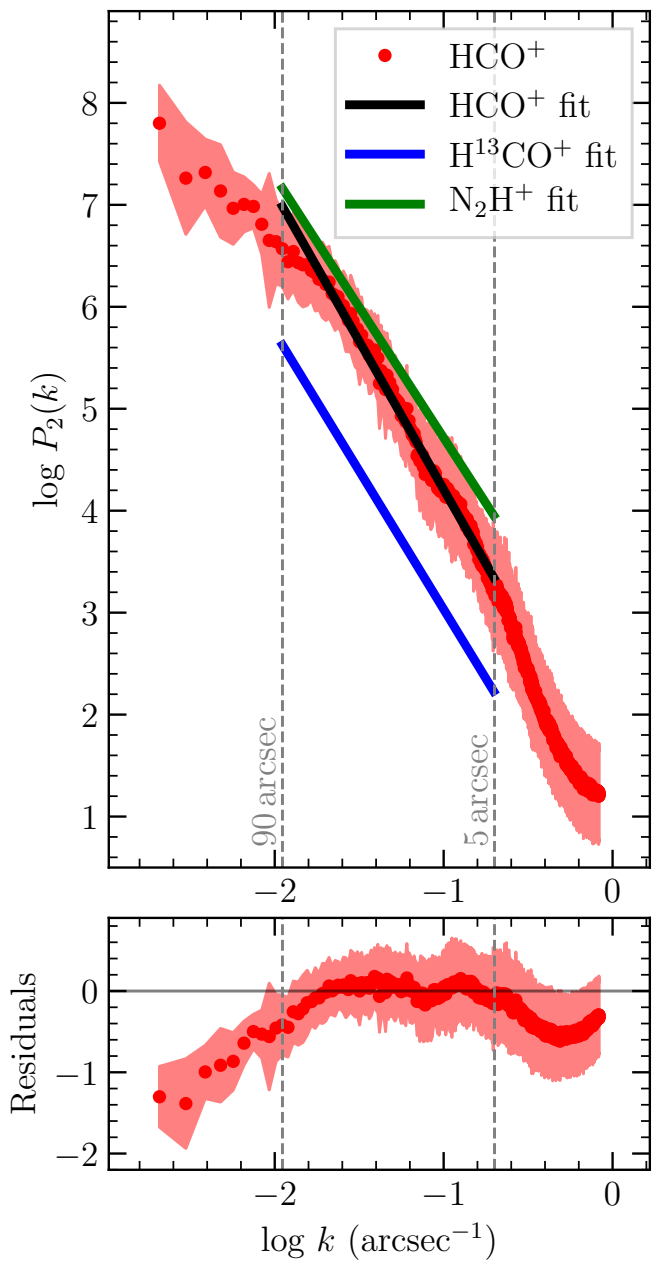

Fig. 16. Power spectra derived in DR20 for $HCO^+(1-0)$, $H^{13}CO^+(1-0)$ and $N_2H^+(1-0)$. The dots and colored area correspond to the HCO^+ data and their 1σ uncertainty. The black line is the fit to the data between 5″ and 90″. For comparison, we show the fits to the corresponding $H^{13}CO^+$ and N_2H^+ in blue and green. The bottom panel presents the residuals of the HCO^+ fit.

regions (e.g., Pingel et al. 2018 and references therein). Since the DR20 region is an active star-forming region, flatter slopes caused by the collapse of the gas and hence dominating gravity are very plausible.

7. Conclusions and summary

We presented the outline, scope, and initial results from the large Max Planck IRAM Observatory Program (MIOP) on star formation in Cyg X (CASCADE). Using the the two IRAM facilities NOEMA and the 30 m telescope, we mapped large mosaics in the Cyg X region in the 3 mm wavelength band in the continuum and spectral line emission. A typical angular resolution of ~ 3″ results in linear resolution elements of < 5000 au. Because the data are complemented by the short-spacing observations of the 30 m telescope, this unique new dataset allowed us to investigate the physical and chemical processes during star formation from large cloud scales down to our spatial resolution limit. Furthermore, covering a plethora of spectral lines and continuum emission, we studied a diverse set of phenomena covering accretion flows from large to small scales, cloud collapse, filamentary structures, and the physical and chemical properties of the gas associated with this prototypical large star formation complex.

After outlining the background and scope of the program, we described the observational setup of the project. Furthermore, we presented the data and analysis of the first observed subarea, namely the DR20 star-forming region, to highlight first results as well as the potential of the entire survey.

The DR20 covers a range of evolutionary stages, and the diverse set of spectral lines allowed us to trace different physical and chemical properties. We identified several velocity components that may stem from accretion flows onto the most massive central star-forming gas clump and from gas that can be affected by the evolving HII region. Employing the HCN/HNC intensity ratio, we derived a large-scale gas temperature map of the region and set it into context with temperatures derived at lower angular resolution from Herschel far-infrared data (Marsh et al. 2017). Furthermore, we explored how much the rarer isotopolog ratio $H^{13}CN/HN^{13}C$ may potentially be used complementary in the highest column density parts of these star-forming regions. An analysis of the DCO^+ emission showed that its emission is almost exclusively identified in cold regions with gas temperatures below 20 K. In addition to this, we investigated the slope of the power spectra for the dense gas tracers HCO^+, $H^{13}CO^+$, and N_2H^+. While the slope of the power spectra in a purely turbulence-dominated regime typically observed for example in HI emission is $-11/3$, optical depth effects can flatten it up to -3. For the dense gas tracers investigated here, we found slopes of -2.9, -2.7, and -2.6, respectively. These flatter slopes are expected for increased Mach numbers and/or self-gravity that becomes dominant compared to the initial turbulent conditions. Because the DR20 region is actively forming stars and is hence dominated by gravity, the flatter slopes of the power spectra agree with the physical status of the region.

The analysis of this initial DR20 dataset outlines the enormous potential of this MIOP on star formation in Cygnus X. CASCADE will allow us detailed investigation of the different physical and chemical aspects and their interrelations from the scale of the natal molecular cloud down to the scale of accretion on the individual protostellar cores.

Acknowledgements. The authors are grateful to the staff at the NOEMA and Pico Veleta observatories for their support of these observations. We thank in particular P. Chaudet, operator at the NOEMA observatory, for his motivation and dedication in developing and testing the advanced mosaic observing procedures employed in this project. This work is based on observations carried out under project number L19MA with the IRAM NOEMA Interferometer and [145-19] with the 30 m telescope. IRAM is supported by INSU/CNRS (France), MPG (Germany) and IGN (Spain). We like to thank Alvaro Hacar, Blakesley Burkhart and Eric Koch for stimulating discussions about the HCN/HNC temperature and the power spectra fitting, respectively. H.B. and S.S. acknowledge support from the European Research Council under the Horizon 2020 Framework Program via the ERC Consolidator Grant CSF-648505. H.B. also acknowledges support from the Deutsche Forschungsgemeinschaft in the Collaborative Research Center (SFB 881) "The Milky Way System" (subproject B1).

References

Albertsson, T., Semenov, D. A., Vasyunin, A. I., Henning, T., & Herbst, E. 2013, ApJS, 207, 27
André, P., Di Francesco, J., Ward-Thompson, D., et al. 2014, in Protostars and Planets VI, ed. H. Beuther, R. Klessen, C. Dullemond, & T. Henning, 27–51
Arzoumanian, D., André, P., Didelon, P., et al. 2011, A&A, 529, L6
Beerer, I. M., Koenig, X. P., Hora, J. L., et al. 2010, ApJ, 720, 679
Beuther, H., Bihr, S., Rugel, M., et al. 2016, A&A, 595, A32
Beuther, H., Gieser, C., Suri, S., et al. 2021, A&A, 649, A113
Beuther, H., Wang, Y., Soler, J., et al. 2020, A&A, 638, A44
Bonnell, I. A. & Bate, M. R. 2002, MNRAS, 336, 659
Bonnell, I. A., Vine, S. G., & Bate, M. R. 2004, MNRAS, 349, 735
Brunthaler, A., Menten, K. M., Dzib, S. A., et al. 2021, A&A, 651, A85
Burkhart, B. 2021, PASP, 133, 102001
Burkhart, B., Collins, D. C., & Lazarian, A. 2015, ApJ, 808, 48
Burkhart, B., Lazarian, A., Ossenkopf, V., & Stutzki, J. 2013, ApJ, 771, 123
Burkhart, B., Stanimirović, S., Lazarian, A., & Kowal, G. 2010, ApJ, 708, 1204
Cao, Y., Qiu, K., Zhang, Q., & Li, G.-X. 2022, ApJ, 927, 106
Cao, Y., Qiu, K., Zhang, Q., et al. 2019, ApJS, 241, 1
Cao, Y., Qiu, K., Zhang, Q., Wang, Y., & Xiao, Y. 2021, ApJ, 918, L4
Collins, D. C., Kritsuk, A. G., Padoan, P., et al. 2012, ApJ, 750, 13
Downes, D. & Rinehart, R. 1966, ApJ, 144, 937
Draine, B. T. 2011, Physics of the Interstellar and Intergalactic Medium (Princeton Series in Astrophysics)
Elmegreen, B. G. & Scalo, J. 2004, ARA&A, 42, 211
Falceta-Gonçalves, D., Kowal, G., de Gouveia Dal Pino, E., et al. 2015, Highlights of Astronomy, 16, 406
Federrath, C. & Klessen, R. S. 2013, ApJ, 763, 51
Gieser, C., Beuther, H., Semenov, D., et al. 2022, A&A, 657, A3
Hacar, A., Alves, J., Tafalla, M., & Goicoechea, J. R. 2017, A&A, 602, L2
Hacar, A., Bosman, A. D., & van Dishoeck, E. F. 2020, A&A, 635, A4
Hacar, A., Clark S., E., Heitsch, F., et al. 2022, arXiv e-prints, arXiv:2203.09562
Hacar, A., Tafalla, M., Kauffmann, J., & Kovács, A. 2013, A&A, 554, A55
Hennebelle, P. & Falgarone, E. 2012, A&A Rev., 20, 55
Hildebrand, R. H. 1983, QJRAS, 24, 267
Jackson, J. M., Rathborne, J. M., Shah, R. Y., et al. 2006, ApJS, 163, 145
Kauffmann, J., Bertoldi, F., Bourke, T. L., Evans, N. J., I., & Lee, C. W. 2008, A&A, 487, 993
Kirk, H., Myers, P. C., Bourke, T. L., et al. 2013, ApJ, 766, 115
Koch, E. W., Rosolowsky, E. W., Boyden, R. D., et al. 2019, AJ, 158, 1
Kolmogorov, A. 1941, Akademiia Nauk SSSR Doklady, 30, 301
Körtgen, B., Bovino, S., Schleicher, D. R. G., Giannetti, A., & Banerjee, R. 2017, MNRAS, 469, 2602
Kumar, M. S. N. & Grave, J. M. C. 2007, A&A, 472, 155
Kumar, M. S. N., Palmeirim, P., Arzoumanian, D., & Inutsuka, S. I. 2020, A&A, 642, A87
Larson, R. B. 2003, Reports on Progress in Physics, 66, 1651
Lazarian, A. & Pogosyan, D. 2000, ApJ, 537, 720
Lazarian, A. & Pogosyan, D. 2004, ApJ, 616, 943
Lazarian, A., Pogosyan, D., & Esquivel, A. 2002, in Astronomical Society of the Pacific Conference Series, Vol. 276, Seeing Through the Dust: The Detection of HI and the Exploration of the ISM in Galaxies, ed. A. R. Taylor, T. L. Landecker, & A. G. Willis, 182
Li, G.-X., Cao, Y., & Qiu, K. 2021, ApJ, 916, 13
Marsh, K. A., Whitworth, A. P., & Lomax, O. 2015, MNRAS, 454, 4282
Marsh, K. A., Whitworth, A. P., Lomax, O., et al. 2017, MNRAS, 471, 2730
Minier, V., Ellingsen, S. P., Norris, R. P., & Booth, R. S. 2003, A&A, 403, 1095
Miville-Deschênes, M. A., Joncas, G., Falgarone, E., & Boulanger, F. 2003, A&A, 411, 109
Molinari, S., Merello, M., Elia, D., et al. 2016a, ApJ, 826, L8
Molinari, S., Schisano, E., Elia, D., et al. 2016b, A&A, 591, A149
Molinari, S., Swinyard, B., Bally, J., et al. 2010, A&A, 518, L100
Motte, F., Bontemps, S., & Louvet, F. 2018, ARA&A, 56, 41
Motte, F., Bontemps, S., Schilke, P., et al. 2007, A&A, 476, 1243
Motte, F., Zavagno, A., Bontemps, S., et al. 2010, A&A, 518, L77+
Myers, P. C., Mardones, D., Tafalla, M., Williams, J. P., & Wilner, D. J. 1996, ApJ, 465, L133
Oliveira, C. M., Hébrard, G., Howk, J. C., et al. 2003, ApJ, 587, 235
Ortiz-León, G. N., Menten, K. M., Brunthaler, A., et al. 2021, A&A, 651, A87
Ossenkopf, V. & Henning, T. 1994, A&A, 291, 943
Panopoulou, G. V., Psaradaki, I., Skalidis, R., Tassis, K., & Andrews, J. J. 2017, MNRAS, 466, 2529
Parise, B., Leurini, S., Schilke, P., et al. 2009, A&A, 508, 737
Peretto, N., Fuller, G. A., André, P., et al. 2014, A&A, 561, A83
Pety, J., Goicoechea, J. R., Hily-Blant, P., Gerin, M., & Teyssier, D. 2007, A&A, 464, L41
Pillai, T., Caselli, P., Kauffmann, J., et al. 2012, ApJ, 751, 135
Pingel, N. M., Lee, M.-Y., Burkhart, B., & Stanimirović, S. 2018, ApJ, 856, 136
Reipurth, B., ed. 2008, Star Formation and Young Clusters in Cygnus, ed. B. Reipurth, Vol. 4, 36
Rygl, K. L. J., Brunthaler, A., Sanna, A., et al. 2012, A&A, 539, A79
Schneider, N., Bontemps, S., Simon, R., et al. 2006, A&A, 458, 855
Schneider, N., Csengeri, T., Bontemps, S., et al. 2010, A&A, 520, A49
Schuller, F., Menten, K. M., Contreras, Y., et al. 2009, A&A, 504, 415
Shirley, Y. L. 2015, PASP, 127, 299
Sousbie, T. 2011, MNRAS, 414, 350
Sousbie, T., Pichon, C., & Kawahara, H. 2011, MNRAS, 414, 384
Stahler, S. W. & Palla, F. 2005, The Formation of Stars (ISBN 3-527-40559-3. Wiley-VCH)
Stanimirović, S. & Lazarian, A. 2001, ApJ, 551, L53
Suri, S., Sánchez-Monge, Á., Schilke, P., et al. 2019, A&A, 623, A142
Taylor, A. R., Gibson, S. J., Peracaula, M., et al. 2003, AJ, 125, 3145
Tobin, J. J., Hartmann, L., Bergin, E., et al. 2012, ApJ, 748, 16
van der Walt, S. J., Kristensen, L. E., Jørgensen, J. K., et al. 2021, A&A, 655, A86
Vázquez-Semadeni, E., Gómez, G. C., Jappsen, A. K., Ballesteros-Paredes, J., & Klessen, R. S. 2009, ApJ, 707, 1023
Vázquez-Semadeni, E., Palau, A., Ballesteros-Paredes, J., Gómez, G. C., & Zamora-Avilés, M. 2019, MNRAS, 490, 3061
von Weizsäcker, C. F. 1951, ApJ, 114, 165
Walsh, A. J., Bourke, T. L., & Myers, P. C. 2006, ApJ, 637, 860
Wang, Y., Beuther, H., Rugel, M. R., et al. 2020, A&A, 634, A83
Zhou, S. 1992, ApJ, 394, 204

Appendix A: Additional figures and line table

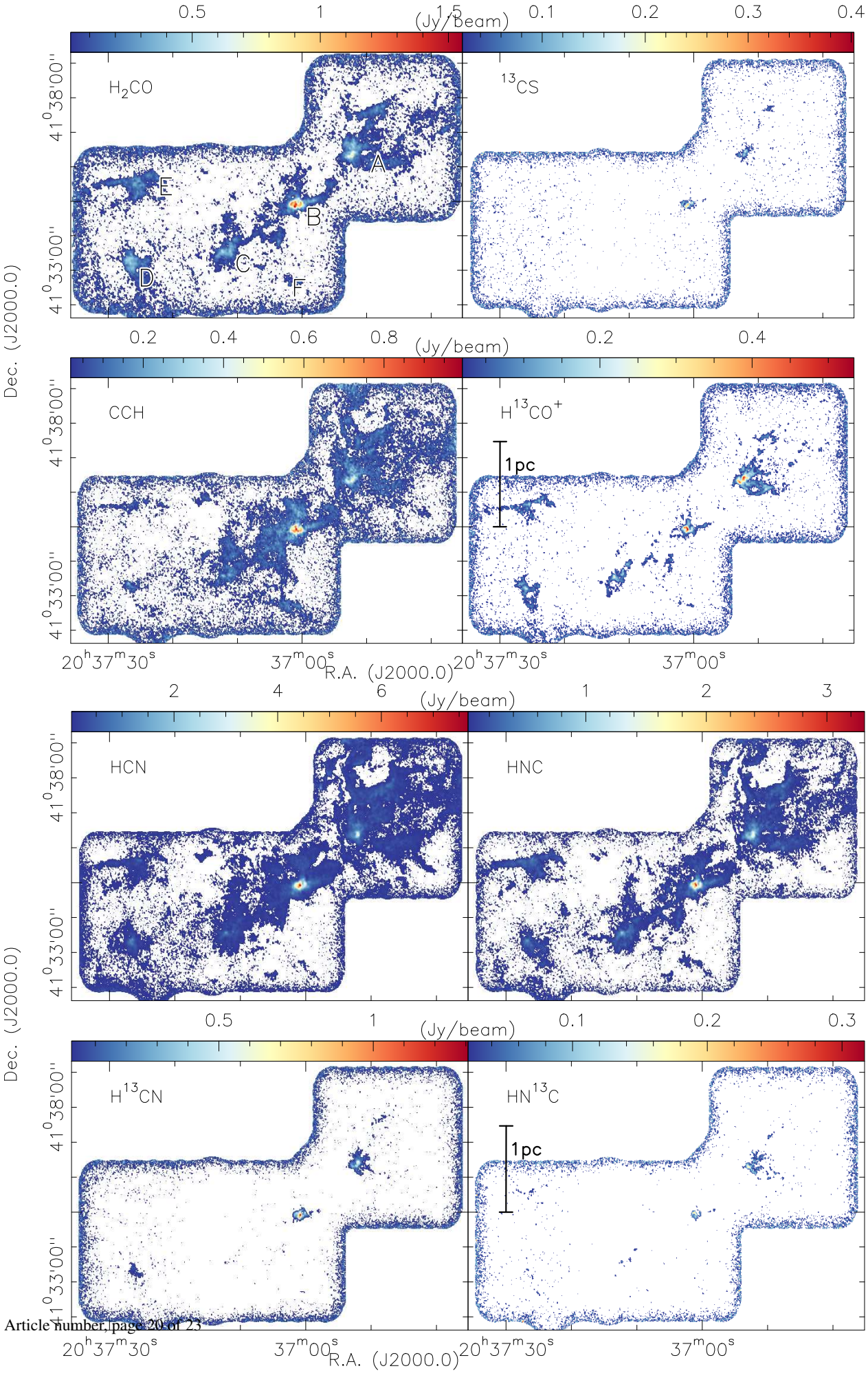

Fig. A.1. Integrated intensities for the species marked in each panel. The integration ranges are always from −7 to 3 km s^{-1}. Only for HCN and H^{13}CN were broader integration ranges from −14 to 8 km s^{-1} used to cover all hyperfine structures of the line. The data were clipped below the 4σ level for each species (Table 1).

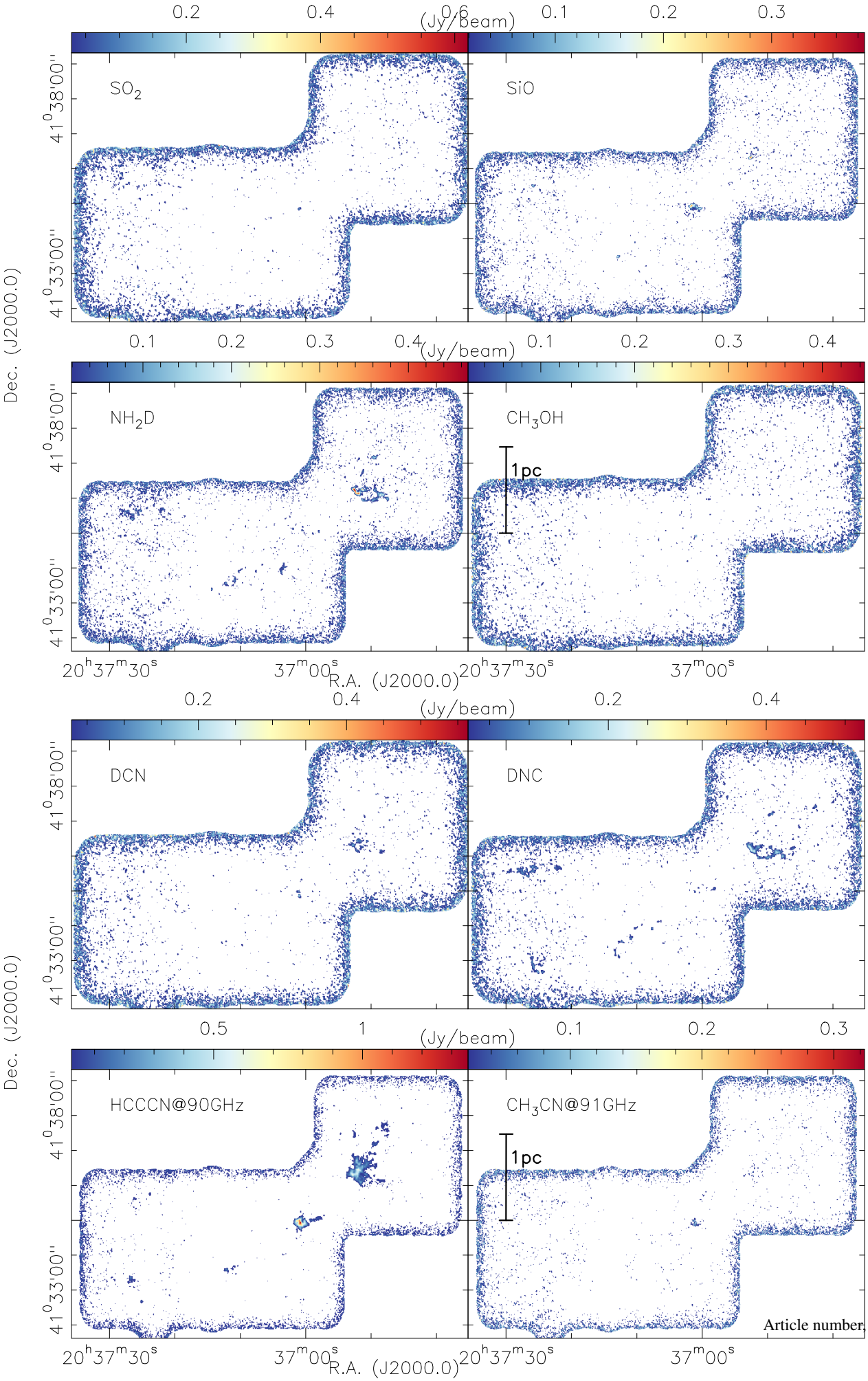

Fig. A.2. Integrated intensities for the species marked in each panel. The integration ranges are always from -7 to 3 km s^{-1}. The data were clipped below the 4σ level for each species (Table 1).

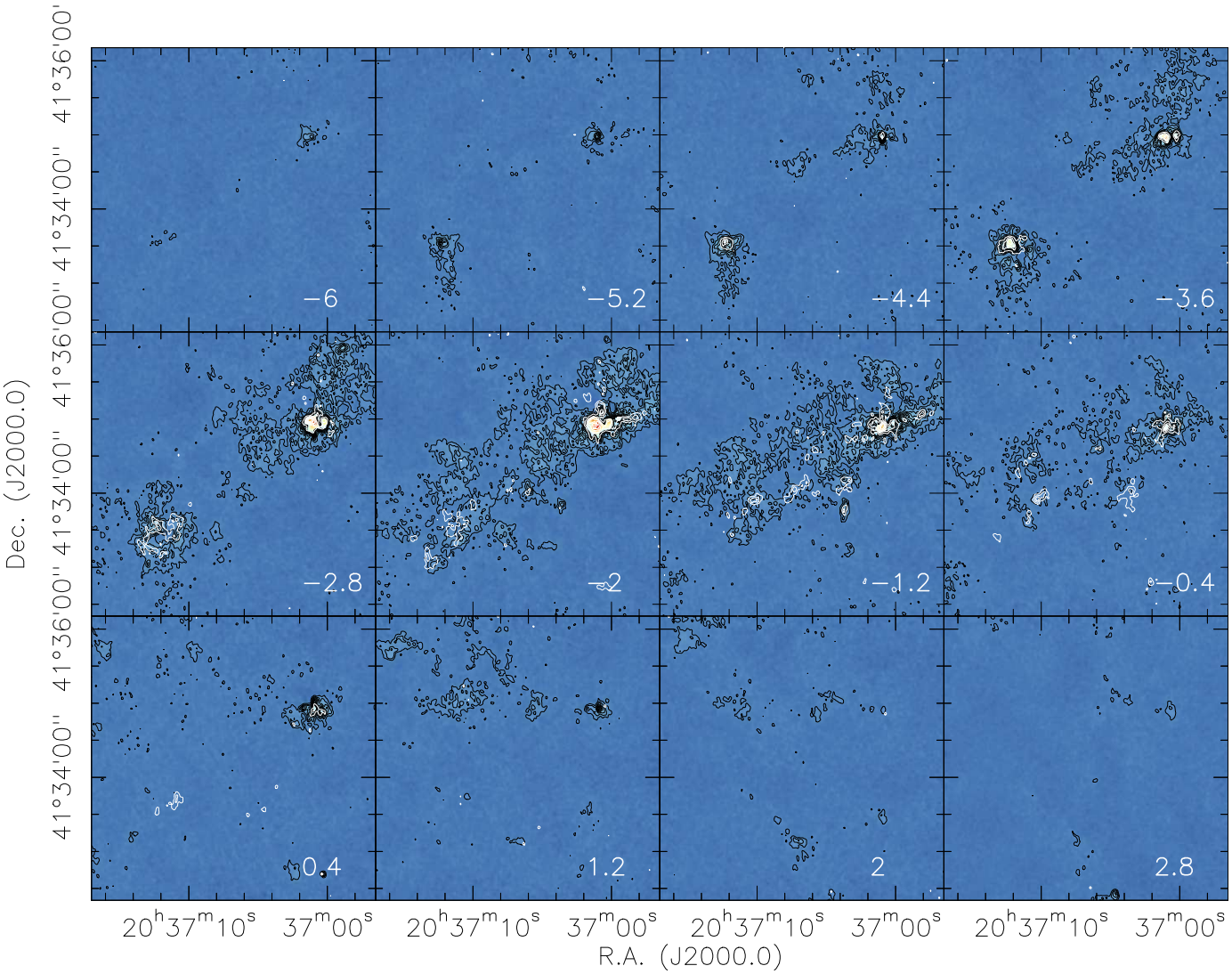

Fig. A.3. Channel maps of the central third of DR20 in the $HCO^+(1-0)$ and $H^{13}CO^+(1-0)$ emission lines. The color and black contours show the $HCO^+(1-0)$ emission, whereas the white contours present the $H^{13}CO^+(1-0)$. Contour levels are always in 5σ steps, and the central velocity is marked in each panel.

Table A.1. Spectral correlator settings with targeted lines.

cent. freq. (GHz)	SB	width (MHz)	Δv (MHz)	frequencies and molecules (MHz)
72.246	LSB	4064	2.00	wideband
76.307	LSB	4064	2.00	wideband
87.733	USB	4064	2.00	wideband
91.795	USB	4064	2.00	wideband
71.909	LSB	64	0.06	71889.741 HC_5N
72.037	LSB	64	0.06	72039.303 DCO^+
72.101	LSB	64	0.06	72107.7205 CCD
72.165	LSB	64	0.06	72156.5915527 72177.6297913
72.421	LSB	64	0.06	72414.905 DCN, 72409.090 H_2CO
72.485	LSB	64	0.06	72475.075 $HC^{13}CCN$, 72482.060 $HCC^{13}CN$, 72409.090 H_2CO
72.741	LSB	64	0.06	72758.243 SO_2
72.805	LSB	64	0.06	72783.822 HCCCN, 72837.948 H_2CO
72.869	LSB	64	0.06	72837.948 H_2CO
72.996	LSB	64	0.06	72976.779 OCS
73.572	LSB	64	0.06	73590.218 CH_3CN
74.084	LSB	64	0.06	74111.42 $HCNH^+$
74.148	LSB	64	0.06	74111.42 $HCNH^+$
74.660	LSB	64	0.06	74644.568 H44α
74.852	LSB	64	0.06	74869.0231934 HC5N
74.916	LSB	64	0.06	74891.677 74924.134 CH_3CHO, 74939.624 H55β
75.812	LSB	64	0.06	75816.443 CH_3SH
75.876	LSB	64	0.06	75864.405 75862.859 CH_3SH
75.940	LSB	64	0.06	75925.914 CH_3SH
76.132	LSB	64	0.06	76117.432 76156.028 C_4H
76.324	LSB	64	0.06	76305.727 DNC
76.516	LSB	64	0.06	76509.684 CH_3OH
76.836	LSB	64	0.06	76838.932 CH_3NH_2
76.900	LSB	64	0.06	76878.952 CH_3CHO
77.028	LSB	64	0.06	77038.605 CH_3CHO
77.092	LSB	64	0.06	77082.951 CH_3CHO, 77109.632 N_2D^+
77.156	LSB	64	0.06	77125.695 CH_3CHO
77.220	LSB	64	0.06	77214.359 HC_5N
77.732	LSB	64	0.06	77731.711 CCS,
85.924	USB	64	0.06	85926.270 NH_2D
86.052	USB	64	0.06	86054.961 $HC^{15}N$
86.308	USB	64	0.06	86338.7367 86340.1764 86342.2551 $H^{13}CN$
86.372	USB	64	0.06	86338.7367 86340.1764 86342.2551 $H^{13}CN$
86.692	USB	64	0.06	86670.760 86708.360 HCO
86.756	USB	64	0.06	86754.288 $H^{13}CO^+$
86.820	USB	64	0.06	86846.960 SiO
86.884	USB	64	0.06	87863.916 HC_5N
87.076	USB	64	0.06	87090.735 87090.859 87090.942 $HN^{13}C$
87.332	USB	64	0.06	87316.925 87328.624 CCH
87.396	USB	64	0.06	87402.004 87407.165 CCH
87.844	USB	64	0.06	87848.855 NH_2CHO
87.908	USB	64	0.06	87925.252 HNCO
88.612	USB	64	0.06	88631.847 HCN
88.868	USB	64	0.06	88851.607 88843.187 CH_3OCHO, 88865.715 $H^{15}NC$
89.188	USB	64	0.06	89188.52470 HCO^+, 88166.806 $H^{13}CCCN$
90.532	USB	64	0.06	90526.205 HC_5N
90.596	USB	64	0.06	90593.061 $HC^{13}CCN$
90.660	USB	64	0.06	90663.593 HNC, 90686.381 CCS
90.788	USB	64	0.06	90771.550 SiS
90.980	USB	64	0.06	90979.023 HCCCN
91.172	USB	64	0.06	91171.039 HDCS
91.940	USB	64	0.06	91987.088 CH_3CN
92.004	USB	64	0.06	91987.088 CH_3CN
92.068	USB	64	0.06	92070.28 HCCCCN, 92075.51 CH_3OD
92.452	USB	64	0.06	92426.248 CH_2CHCN, 92494.308 ^{13}CS
92.516	USB	64	0.06	92494.308 ^{13}CS
93.156	USB	64	0.06	93173.777 N_2H^+